Journal of Computational Applied Mechanics 2027, 58(1): 111-139
DOI: 10.22059/jcamech.2026.426800.2023

RESEARCH PAPER

Size and Surface Effects on the Dynamic Stability of Immersed Sandwich Micro/Nanoplates with Functionally Graded Face Sheets and an FG-TPMS Core

Yang Yang [a, b, c], Lulu Cheng [b, d], Wei Chen [e], Peng Shi [b, c, *], Haoge Shou [b, c]

[a] *Zhumadian Second People's Hospital, the Affiliated Encephalopathy Hospital of Zhengzhou University, Henan, PR China*
[b] *School of Intelligent Manufacturing, Huanghuai University, Zhumadian, Henan, PR China*
[c] *Zhumadian Key Laboratory of Additive Manufacturing and Special Processes, Henan, PR China*
[d] *Zhumadian Central Hospital, Zhumadian, Henan, PR China*
[e] *School of Civil Engineering, University of South China, Hengyang, PR China*

Abstract

The static buckling and principal parametric instability of a sandwich micro/nanoplate submerged in an ideal fluid are investigated. The plate has a functionally graded triply periodic minimal surface (FG-TPMS) core and two face sheets graded from aluminium at the core interfaces to silicon at the outer surfaces. A five-variable higher order plate theory is used with the modified couple stress theory (MCST) and the Gurtin-Murdoch (GM) surface model. The governing equations are discretised by isogeometric analysis. Fluid inertia is included through equivalent added mass for horizontal and vertical immersion, and the principal instability boundaries are obtained by first harmonic balance. The results are checked against published benchmarks and a mesh convergence study. For the reference plate, the net GM contribution slightly raises the critical buckling load and the two instability boundaries. Increasing the MCST length raises the excitation frequencies, while increasing immersion lowers them. Additionally, increasing the face gradient exponent reduces the mean silicon content and lowers both boundaries.

Keywords: FG-TPMS core; Functionally graded faces; Dynamic stability; Isogeometric analysis; Modified couple stress theory; Surface elasticity; Fluid added mass

1. Introduction

Functionally graded triply periodic minimal surface (FG-TPMS) architectures allow the distribution of solid material to be tailored within a continuous periodic geometry. Their high specific stiffness, large internal surface area, and interconnected pores make them attractive for lightweight load bearing components, heat exchangers, acoustic liners, energy absorbers, and multifunctional devices. These advantages are supported by effective property studies and additive manufacturing investigations that have clarified how topology, relative density, and manufacturing resolution govern the macroscopic response. In many applications, however, the architected core is not used alone. It is enclosed by dense face sheets to form a sandwich plate, and the structure may operate in water, coolant, or another surrounding liquid while being subjected to compressive and time periodic in plane loads. The resulting dynamic stability problem requires the structural, scale, surface, and fluid contributions to be represented within one formulation. The influence of TPMS grading on structural response has been examined in beams, plates and shells [1-

* Corresponding author. *E-mail address:* pengshi@huanghuai.edu.cn

3]. Viet and Zaki [1] investigated free vibration and buckling of graded TPMS beams. Nguyen-Xuan et al. [2] formulated a model for FG-TPMS plates, while Nguyen et al. [3] used isogeometric analysis for FG-TPMS shells. Feng et al. [4] studied the design and optimisation of sandwich panels with TPMS cores. In a sandwich plate, the face sheets and core contribute differently to bending stiffness and mass. Their properties must therefore be integrated separately when the objective is to determine the effect of changing the face composition or core thickness.

The analysis of an immersed sandwich plate requires a description of both the layered structure and the inertia of the surrounding liquid. El Meiche et al. [5] used a hyperbolic shear deformation theory to study buckling and vibration of functionally graded sandwich plates. Shi et al. [6] solved the mechanical buckling problem by a deep energy method with normalised hard constraints. For submerged plates, the fluid also contributes to the inertia. Soni et al. [7] studied the vibration of submerged plates, and Yildizdag et al. [8] used a coupled isogeometric finite element and boundary element method for partially submerged plates. Ramian et al. [9] considered sandwich plates with a compressible core in contact with fluid, while Pham et al. [10] examined bidirectionally graded plates in a fluid medium. Chen et al. [11] used a higher order isogeometric formulation for thermal vibration of graded porous microplates in an ideal fluid. The fluid domain differs between horizontal and vertical immersion, so the added mass must be evaluated for each configuration.

As the plate thickness approaches the material length scale, the classical plate model may no longer capture the dependence of the response on thickness. Yang et al. [12] introduced the modified couple stress theory (MCST), which requires one material length parameter. Kim et al. [13] applied this theory to bending, free vibration and buckling of graded porous microplates. Fan et al. [14] used a NURBS formulation to study geometrically nonlinear oscillations of such plates. Thanh et al. [15] considered size effects in thermal stability, whereas Pham and Nguyen [16] investigated dynamic stability under periodic in-plane compression. For FG-TPMS plates, Nguyen et al. [17] developed an isogeometric microplate model and Phung-Van et al. [18] used nonlocal strain gradient theory to examine nanoscale response. Hung et al. [19] subsequently considered graphene-reinforced FG-TPMS microplates. These studies address the effect of material length on structural response, mainly in the absence of a surrounding fluid.

While MCST introduces a material length into the bulk constitutive model, the outer faces can contribute to the plate response through their own stresses and elasticity. Gurtin and Murdoch [20] described a material surface as a continuum with its own stress and elastic properties. Lu et al. [21] included surface energy in Kirchhoff and Mindlin plate models. Malekzadeh and Shojaee [22] examined nanoplate vibration with surface and nonlocal effects, and Zhou et al. [23] developed a third-order plate model from the GM theory. Surface stresses have also been considered in nanoplate buckling and primary resonance [24, 25]. For a sandwich plate, the two outer surfaces lie farthest from the midplane, so their contribution to bending differs from that of the material distributed through the face sheets.

Because both mechanisms can affect the response of thin plates, several studies have incorporated bulk size effects and surface energy within the same formulation [26-30]. Shaat et al. [26] used MCST to analyse the bending of Kirchhoff nanoplates with surface effects. Lu et al. [29] combined surface energy with nonlocal strain gradient theory. Using a third-order shear deformation model, Shi et al. [31] investigated bending, vibration and buckling of graded porous microplates with both MCST and GM terms. Nguyen and Phan [32] examined dynamic instability of thin nanoplates with size and surface effects. Khorshidi et al. [33] considered a different part of the problem, namely the natural frequencies of submerged microplates in modified strain gradient theory. Fluid interaction has also been studied for piezoelectric nanoplates [34].

The studies reviewed above leave open how bulk size effects and surface elasticity influence the principal instability boundaries of an immersed sandwich plate with an FG-TPMS core. Therefore, the present study considers a submerged sandwich micro/nanoplate with Al-Si face sheets and an Al FG-TPMS core under periodic biaxial compression. Each face is graded from aluminium next to the core to silicon at the outer surface. A five-variable higher order plate model is discretised by isogeometric analysis. MCST is used for the bulk size effect, and fluid inertia is represented by equivalent added mass for horizontal and vertical immersion. The two boundaries of the first principal instability region are calculated with first harmonic balance. Comparisons with and without the surface and couple stress terms are made at otherwise identical inputs.

The remainder of the paper is organised as follows. Section 2 presents the plate model, the material distributions and the governing equations. Section 3 describes the isogeometric discretisation and the calculation of the instability boundaries. Section 4 gives the convergence study and benchmark comparisons. The numerical results for immersion, plate thickness, material length, preload and sandwich composition are discussed in Section 5. Section 6 gives the conclusions.

2. Formulation

2.1 Physical model and coordinate system

The geometry of the submerged sandwich plate is shown in Fig. 1. The three-dimensional plate domain is defined by

$$\mathcal{V}=\left\{(x,y,z)|0\le x\le a,0\le y\le b,-H/2\le z\le H/2\right\} \tag{1}$$

where x and y are the in plane Cartesian coordinates, z is the thickness coordinate measured from the reference midplane, a and b are the plate length and width, respectively, and H is the total thickness. To identify the two face sheets, the graded porous core, and the two external material surfaces, the thickness interval in Eq. (1) is divided as

$$H=2h_f+h_c,\quad S^{\pm}:z=\pm\frac{H}{2} \tag{2}$$

Here, h_f is the thickness of each face sheet, h_c is the core thickness. The coordinates S^+ and S^- identify the external top and bottom GM surfaces, respectively. Perfect bonding is imposed at $z=-h_c/2$ and $z=+h_c/2$, and no independent surface layer is assigned to either internal interface. The surrounding liquid is assumed not to penetrate the porous core, and fluid motion within the TPMS pores is therefore excluded. The GM surface model is applied only to the top and bottom external faces of the plate. Surface energy associated with the internal TPMS pore walls is neglected.

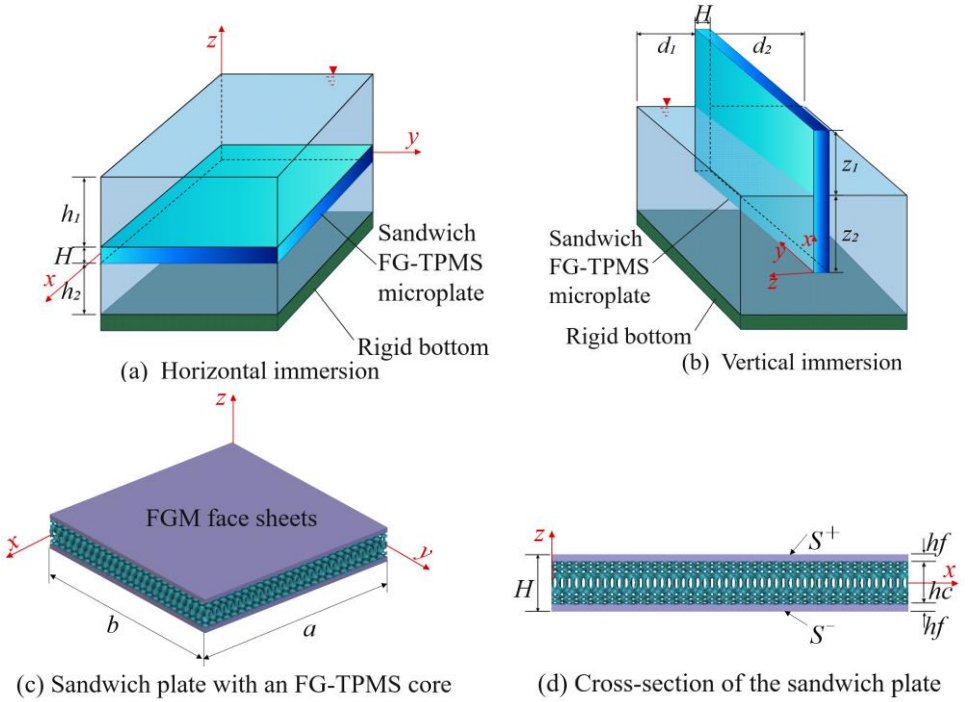


Fig 1: Physical model of the sandwich micro/nanoplate with an FG-TPMS core interacting with an ideal fluid. The face sheets grade from aluminium at the core interfaces to silicon at the external surfaces.

2.2 Material properties of the FG-TPMS core and Al–Si face sheets

In the present study, the FG-TPMS core has an IWP (Igraph and Wrapped Package-graph) topology. Its periodic surface is defined by

$$\begin{aligned}\phi(x,y,z)=&\,2\cos(\kappa_1x)\cos(\kappa_2y)+2\cos(\kappa_2y)\cos(\kappa_3z)+2\cos(\kappa_3z)\cos(\kappa_1x)\\&-\cos(2\kappa_1x)-\cos(2\kappa_2y)-\cos(2\kappa_3z)\end{aligned} \tag{3}$$

where $\phi(x,y,z)$ is a prescribed level set that defines the minimal surface topology. The scaled coordinates appearing in Eq. (3) are

$$\kappa_i = \frac{2\pi t_i}{l_i}, \quad i = 1,2,3 \tag{4}$$

in which l_i is the unit cell length and t_i is the number of unit cells along the corresponding coordinate direction.

The local solid volume fraction, which is also the relative density of the porous core, is defined as

$$V = \frac{V^{TPMS}}{V^m} \tag{5}$$

where V^m is the volume occupied by the base material and V^{TPMS} is the volume of the TPMS unit cell.

The through thickness variation of the local volume fraction in Eq. (5) is prescribed by

$$V = \left(V_{\max} - V_{\min}\right) V^{pattern} + V_{\min} \tag{6}$$

Accordingly, the selected TPMS distribution pattern is written as

$$V^{pattern}(z) = \left(1 - \cos\left(\frac{\pi z}{h_c}\right)\right)^n, \quad |z| \le \frac{h_c}{2} \tag{7}$$

Table 1 summarizes the homogenized elastic properties of the FG-TPMS (IWP) core. Table 2 lists the parameters that define the selected distribution with an average relative density of 0.35.

Table 1: Effective mechanical properties of the FG-TPMS (IWP) core [2].

Model	Material properties	V
IWP TPMS	$E(z) = E^m \begin{cases} 0.597V^{1.225} \\ 0.987V^{1.782} + 0.013 \end{cases}$	$\begin{cases} V \le 0.35 \\ V > 0.35 \end{cases}$
	$G(z) = G^m \begin{cases} 0.529V^{1.287} \\ 0.960V^{2.188} + 0.040 \end{cases}$	$\begin{cases} V \le 0.35 \\ V > 0.35 \end{cases}$
	$\nu(z) = \begin{cases} 2.597e^{-0.157V} - 2.244 \\ 0.201V^2 - 0.227V + 0.326 \end{cases}$	$\begin{cases} V \le 0.13 \\ V > 0.13 \end{cases}$

Table 2: Parameters of the FG-TPMS distribution with an average relative density of 0.35 [2].

Parameters	value
n	3.943
$V_{\min}$	0.25
$V_{\max}$	1.0

The relative density determines the effective properties of the FG-TPMS core, whereas the constituent volume fractions determine the local properties of the Al-Si face sheets. The composition of the two face sheets is symmetric about the plate midplane. The silicon volume fraction in either face is $V_{\mathrm{Si}} = \left[(|z| - h_c/2)/h_f\right]^{p_f}$, where $p_f > 0$ is the face gradient exponent. The aluminium fraction is $1 - V_{\mathrm{Si}}$. This distribution gives aluminium at the face-core interfaces and silicon at the two outer surfaces. The Young's modulus, Poisson's ratio and mass density, denoted collectively by $P \in \{E, \nu, \rho\}$, are evaluated by the volume fraction mixture law $P_f = (1 - V_{\mathrm{Si}})P_{\mathrm{Al}} + V_{\mathrm{Si}}P_{\mathrm{Si}}$.

2.3 Five variable higher order kinematics and strain field

The five variable displacement field follows the higher order plate model in [35]. Its independent generalized variables are collected as

$$\mathbf{d}(x,y,t)=\left(u,\ v,\ w,\ \theta_x,\ \theta_y\right)^{\mathrm{T}} \tag{8}$$

in which *u*, *v* and *w* are the in plane and transverse displacements, respectively; θ_x and θ_y are rotations of normal to the midplane about *y* and *x* axis. At an arbitrary material point, the three dimensional displacements are

$$\begin{aligned} U(x,y,z,t)&=u-zw_{,x}+f(z)\theta_x \\ V(x,y,z,t)&=v-zw_{,y}+f(z)\theta_y \\ W(x,y,z,t)&=w \end{aligned} \tag{9}$$

Here, $U, V,$ and W are the physical displacement components and $f(z)$ is the shear deformation shape function:

$$f(z)=z-\frac{4z^3}{3H^2} \tag{10}$$

The strain components are given by:

$$\varepsilon_{xx}=U_{,x},\quad \varepsilon_{yy}=V_{,y},\quad \gamma_{xy}=U_{,y}+V_{,x} \tag{11}$$

$$\gamma_{xz}=U_{,z}+W_{,x},\quad \gamma_{yz}=V_{,z}+W_{,y},\quad \varepsilon_{zz}=W_{,z}=0 \tag{12}$$

Here, a comma denotes a spatial derivative, and the shear strains are engineering components. Substituting Eqs. (9) and (10) into Eqs. (11) and (12) gives

$$\boldsymbol{\varepsilon}_p=\boldsymbol{\varepsilon}_1+z\boldsymbol{\varepsilon}_2+f(z)\boldsymbol{\varepsilon}_3,\qquad \boldsymbol{\gamma}_s=f'(z)\boldsymbol{\theta} \tag{13}$$

$$\begin{aligned} \boldsymbol{\varepsilon}_1&=\left(u_{,x}\ \ v_{,y}\ \ u_{,y}+v_{,x}\right)^{\mathrm{T}} \\ \boldsymbol{\varepsilon}_2&=\left(-w_{,xx}\ \ -w_{,yy}\ \ -2w_{,xy}\right)^{\mathrm{T}} \\ \boldsymbol{\varepsilon}_3&=\left(\theta_{x,x}\ \ \theta_{y,y}\ \ \theta_{x,y}+\theta_{y,x}\right)^{\mathrm{T}} \\ \boldsymbol{\theta}&=\left(\theta_x\ \ \theta_y\right)^{\mathrm{T}} \end{aligned} \tag{14}$$

Thus, only $\boldsymbol{\varepsilon}_1, \boldsymbol{\varepsilon}_2,$ and $\boldsymbol{\varepsilon}_3$ are required for the in plane part, while $\boldsymbol{\theta}$ supplies the transverse shear part.

2.4 Sandwich bulk constitutive law and bulk energies

The in-plane and transverse shear stresses are related to the corresponding strains by

$$\sigma_{xx}^{b}=\frac{E}{1-\nu^2}(\varepsilon_{xx}+\nu\varepsilon_{yy}),\qquad \sigma_{yy}^{b}=\frac{E}{1-\nu^2}(\varepsilon_{yy}+\nu\varepsilon_{xx}) \tag{15}$$

$$\tau_{xy}^{b}=G\gamma_{xy},\quad \tau_{xz}^{b}=G\gamma_{xz},\quad \tau_{yz}^{b}=G\gamma_{yz} \tag{16}$$

The superscript b denotes the bulk stresses before the surface induced correction. Here, E, ν and G are the local Young's modulus, Poisson's ratio and shear modulus, respectively. In the core, the fitted value of G in Table 1 is used independently of E and ν. In the faces, $G=E/[2(1+\nu)]$. Equations (15) and (16) are collected below in vector form.

$$\boldsymbol{\sigma}_p(z)=\mathbf{Q}(z)\boldsymbol{\varepsilon}_p(z),\qquad \boldsymbol{\tau}_s(z)=\mathbf{Q}_s(z)\boldsymbol{\gamma}_s(z) \tag{17}$$

$$\mathbf{Q}(z)=\begin{pmatrix} \dfrac{E}{1-\nu^2} & \dfrac{\nu E}{1-\nu^2} & 0 \\ \dfrac{\nu E}{1-\nu^2} & \dfrac{E}{1-\nu^2} & 0 \\ 0 & 0 & G \end{pmatrix}, \qquad \mathbf{Q}_s(z)=\begin{pmatrix} G(z) & 0 \\ 0 & G(z) \end{pmatrix} \tag{18}$$

In Eqs. (17) and (18), $\boldsymbol{\sigma}_p$ and $\boldsymbol{\tau}_s$ are the in plane and transverse shear stress vectors, and $\mathbf{Q}$ and $\mathbf{Q}_s$ are their constitutive matrices. The complete sandwich is described by the following single piecewise field:

$$\{E(z),\nu(z),\rho(z)\}=\begin{cases}\{E_f(z),\nu_f(z),\rho_f(z)\}, & h_c/2<|z|\le H/2,\\ \{E_c(z),\nu_c(z),\rho_c(z)\}, & |z|\le h_c/2.\end{cases} \tag{19}$$

The subscripts f and c denote the face sheets and the core, respectively. The face properties follow the mixture law in Section 2.2. The core elastic properties are given in Table 1, and the core density is the product of the aluminium density and the local relative density. Substituting the strains in Eq. (13) into Eq. (17) gives the bulk strain energy

$$U_b=\frac{1}{2}\int_{\Omega_p}\int_{-H/2}^{H/2}\left(\boldsymbol{\varepsilon}_p^{\mathrm{T}}\mathbf{Q}\boldsymbol{\varepsilon}_p+\boldsymbol{\gamma}_s^{\mathrm{T}}\mathbf{Q}_s\boldsymbol{\gamma}_s\right)\mathrm{d}z\,\mathrm{d}\Omega_p,\quad \mathrm{d}\Omega_p=\mathrm{d}x\mathrm{d}y \tag{20}$$

The bulk kinetic energy is calculated from the three-dimensional displacement field as

$$T_b=\frac{1}{2}\int_{\Omega_p}\int_{-H/2}^{H/2}\rho(z)\dot{\mathbf{u}}^{\mathrm{T}}\dot{\mathbf{u}}\,\mathrm{d}z\,\mathrm{d}\Omega_p,\qquad \mathbf{u}=\left(U,\ V,\ W\right)^{\mathrm{T}} \tag{21}$$

2.5 Modified couple stress contribution

The modified couple stress theory of Yang et al. [12] introduces a material length into the constitutive law. The rotation, symmetric curvature and couple stress are defined as

$$\boldsymbol{\omega}=\frac{1}{2}\nabla\times\mathbf{u},\qquad \boldsymbol{\chi}=\frac{1}{2}\left(\nabla\boldsymbol{\omega}+\nabla\boldsymbol{\omega}^{\mathrm{T}}\right),\qquad \mathbf{m}=2G(z)\ell^2\boldsymbol{\chi} \tag{22}$$

In Eq. (22), $\boldsymbol{\omega}$ and $\boldsymbol{\chi}$ are the rotation and curvature tensors, $\mathbf{m}$ is the couple stress tensor, and ℓ is the material length scale parameter. Substitution of the displacement field in Eq. (9) first gives the three rotation components

$$\omega_x=w_{,y}-\frac{1}{2}f'\theta_y,\quad \omega_y=-w_{,x}+\frac{1}{2}f'\theta_x,\quad \omega_z=\frac{1}{2}\left(v_{,x}-u_{,y}+f\theta_{y,x}-f\theta_{x,y}\right) \tag{23}$$

Differentiation of the rotations in Eq. (23) gives the following components:

$$\chi_{xx}=w_{,xy}-\tfrac{1}{2}f'\theta_{y,x},\quad \chi_{yy}=-w_{,xy}+\tfrac{1}{2}f'\theta_{x,y} \tag{24}$$

$$\chi_{xy}=\tfrac{1}{2}(w_{,yy}-w_{,xx})+\tfrac{1}{4}f'(\theta_{x,x}-\theta_{y,y}) \tag{25}$$

$$4\chi_{xz}=v_{,xx}-u_{,xy}+f(\theta_{y,xx}-\theta_{x,xy})-f''\theta_y \tag{26}$$

$$4\chi_{yz}=v_{,xy}-u_{,yy}+f(\theta_{y,xy}-\theta_{x,yy})+f''\theta_x \tag{27}$$

In component form the couple stress law in Eq. (22) reads $m_{ij}=2G(z)\ell^2\chi_{ij}$. The components in Eqs. (24)–(27) are grouped by their thickness dependence as follows.

$$\boldsymbol{\chi}_p = \boldsymbol{\chi}_{p1} + f'(z)\boldsymbol{\chi}_{p2}, \qquad \boldsymbol{\chi}_s = \boldsymbol{\chi}_{s1} + f(z)\boldsymbol{\chi}_{s2} + f''(z)\boldsymbol{\chi}_{s3} \tag{28}$$

$$\boldsymbol{\chi}_{p1} = \{w_{,xy}, -w_{,xy}, (w_{,yy} - w_{,xx})/2\}^{\mathrm{T}}, \ \ \boldsymbol{\chi}_{p2} = \{-\theta_{y,x}/2, \theta_{x,y}/2, (\theta_{x,x} - \theta_{y,y})/4\}^{\mathrm{T}} \tag{29}$$

$$\boldsymbol{\chi}_{s1} = \frac{1}{4}\{v_{,xx} - u_{,xy}, v_{,xy} - u_{,yy}\}^{\mathrm{T}}, \ \ \boldsymbol{\chi}_{s2} = \frac{1}{4}\{\theta_{y,xx} - \theta_{x,xy}, \theta_{y,xy} - \theta_{x,yy}\}^{\mathrm{T}}, \ \ \boldsymbol{\chi}_{s3} = \frac{1}{4}\{-\theta_y, \theta_x\}^{\mathrm{T}} \tag{30}$$

The vectors $\boldsymbol{\chi}_p$ and $\boldsymbol{\chi}_s$ contain the three in plane and two transverse curvature components, respectively. Their coefficient vectors in Eqs. (29) and (30) depend only on the five generalized variables and their in plane derivatives. The corresponding vector constitutive equations are:

$$\mathbf{m}_p = \mathbf{Q}_{\mu p}\boldsymbol{\chi}_p, \ \ \mathbf{m}_s = \mathbf{Q}_{\mu s}\boldsymbol{\chi}_s \tag{31}$$

$$\mathbf{Q}_{\mu p} = 2G(z)\ell^2\begin{pmatrix} 1 & 0 & 0 \\ 0 & 1 & 0 \\ 0 & 0 & 2 \end{pmatrix}, \ \ \mathbf{Q}_{\mu s} = 2G(z)\ell^2\begin{pmatrix} 2 & 0 \\ 0 & 2 \end{pmatrix} \tag{32}$$

Here, $\mathbf{m}_p$ and $\mathbf{m}_s$ are the in plane and transverse couple stress vectors. Substituting Eqs. (31) and (32) into the curvature work gives the MCST energy:

$$U_\mu = \frac{1}{2}\int_{\Omega_p}\int_{-H/2}^{H/2}\left(\boldsymbol{\chi}_p^{\mathrm{T}}\mathbf{Q}_{\mu p}\boldsymbol{\chi}_p + \boldsymbol{\chi}_s^{\mathrm{T}}\mathbf{Q}_{\mu s}\boldsymbol{\chi}_s\right)\mathrm{d}z\,\mathrm{d}\Omega_p \tag{33}$$

Like the bulk energy in Eq. (20), Eq. (33) is integrated directly through the three physical material intervals.

2.6 Gurtin and Murdoch surface elasticity, residual stress and surface inertia

In the present study, the surface constants are those assigned to silicon and are the same on both outer faces. The transverse normal stress correction is evaluated with the local bulk Poisson's ratio. Based on the GM model [20], each exposed surface is represented by a membrane of zero thickness bonded to the plate. Substituting the two external surface coordinates into Eq. (13) gives

$$\boldsymbol{\varepsilon}_p^{s,\pm} = \boldsymbol{\varepsilon}_1 + z_\pm\boldsymbol{\varepsilon}_2 + f_\pm\boldsymbol{\varepsilon}_3, \ \ z_+ = H/2, \ \ z_- = -H/2, \ \ f_\pm = f(z_\pm) \tag{34}$$

where $\boldsymbol{\varepsilon}_p^{s,+}$ and $\boldsymbol{\varepsilon}_p^{s,-}$ are the in plane strain vectors of the upper and lower surfaces. The GM constitutive equations are:

$$\begin{aligned} &\sigma_{ij}^{s,\pm} = \tau_s\delta_{ij} + (\lambda_s + \tau_s)\varepsilon_{qq}^{s,\pm}\delta_{ij} + 2(\mu_s - \tau_s)\varepsilon_{ij}^{s,\pm} + \tau_s U_{i,j}^{\pm}, \\ &\tau_{iz}^{s,\pm} = \tau_s w_{,i}, \qquad\qquad i,j,q \in \{x,y\} \end{aligned} \tag{35}$$

$$\boldsymbol{\sigma}_p^{s,\pm} = \mathbf{D}_s\boldsymbol{\varepsilon}_p^{s,\pm} + \tau_s\left(1,\ 1,\ 0\right)^{\mathrm{T}}, \ \ \mathbf{D}_s = \begin{pmatrix} \lambda_s + 2\mu_s & \lambda_s + \tau_s & 0 \\ \lambda_s + \tau_s & \lambda_s + 2\mu_s & 0 \\ 0 & 0 & \mu_s - \tau_s/2 \end{pmatrix} \tag{36}$$

The Latin indices in Eq. (35) run only over the two in plane directions. The three common surface parameters $\lambda_s, \mu_s,$ and τ_s are the two surface Lame constants and the residual surface stress, respectively. $\mathbf{D}_s$ is the surface elastic matrix.

The transverse normal traction is obtained from surface equilibrium. Taking the surface divergence of the transverse components in Eq. (35) gives

$$\sigma_{zz}^{s,+} = \tau_{xz,x}^{s,+} + \tau_{yz,y}^{s,+} = \tau_s\nabla^2 w, \ \ \sigma_{zz}^{s,-} = -\left(\tau_{xz,x}^{s,-} + \tau_{yz,y}^{s,-}\right) = -\tau_s\nabla^2 w \tag{37}$$

A linear interpolation between the two boundary values in Eq. (37) is used for the transverse normal stress through the thickness:

$$\sigma_{zz}(z)=\frac{1}{2}\left(\sigma_{zz}^{s,+}+\sigma_{zz}^{s,-}\right)+\frac{z}{H}\left(\sigma_{zz}^{s,+}-\sigma_{zz}^{s,-}\right),\quad \sigma_{zz}(z)=\frac{2\tau_s z}{H}\nabla^2 w \tag{38}$$

Equation (38) makes the origin of $\sigma_{zz}(z)$ explicit: the two GM surfaces generate the boundary tractions, and only their equilibrium continuation varies through the sandwich. The GM constitutive law itself is not applied to the core or to either face and core interface.

Although the five variable plate kinematics set the transverse normal strain to zero, the stress in Eq. (38) modifies the in plane stress through the Poisson coupling of the bulk material. Substitution into Eq. (17) gives

$$\boldsymbol{\sigma}_p(z)=\mathbf{Q}(z)\boldsymbol{\varepsilon}_p(z)+\mathbf{Q}_z(z)\boldsymbol{\varepsilon}_4 \tag{39}$$

$$\mathbf{Q}_z=\frac{2\nu(z)z\tau_s}{H\left(1-\nu(z)\right)}\begin{pmatrix}1&0&0\\0&1&0\\0&0&0\end{pmatrix},\quad \boldsymbol{\varepsilon}_4=\left(\nabla^2 w,\ \nabla^2 w,\ 0\right)^{\mathrm{T}},\quad \nabla^2=\partial_x^2+\partial_y^2 \tag{40}$$

In the following, $c(z)=2z\tau_s\nu(z)/[H(1-\nu(z))]$ denotes the scalar coefficient of the two identical normal entries in Eq. (40). Thus the increments in the two in plane normal stresses are both $c(z)\nabla^2 w$, and the in plane shear stress is unchanged.

The elastic part of Eq. (36) and the small slope work of the residual surface stress give the combined surface strain energy:

$$U_s=\frac{1}{2}\int_{\Omega_p}\left((\boldsymbol{\varepsilon}_p^{s,+})^{\mathrm{T}}\mathbf{D}_s\boldsymbol{\varepsilon}_p^{s,+}+(\boldsymbol{\varepsilon}_p^{s,-})^{\mathrm{T}}\mathbf{D}_s\boldsymbol{\varepsilon}_p^{s,-}+2\tau_s(\nabla w)^{\mathrm{T}}\nabla w\right)\mathrm{d}\Omega_p \tag{41}$$

The first two terms of Eq. (41) are the elastic energies of the top and bottom membranes; the final term is the gradient energy of the residual stress. The Poisson correction generated by Eqs. (39) and (40) contributes separately to the bulk stress work:

$$U_{zz}=\frac{1}{2}\int_{\Omega_p}\int_{-H/2}^{H/2}\boldsymbol{\varepsilon}_p^{\mathrm{T}}\mathbf{Q}_z\boldsymbol{\varepsilon}_4\,\mathrm{d}z\,\mathrm{d}\Omega_p \tag{42}$$

Equations (41) and (42) therefore separate direct surface elasticity from the induced transverse normal stress correction without introducing surface matrices integrated through the thickness. Finally, the mass carried by the two material surfaces gives

$$T_s=\frac{1}{2}\int_{\Omega_p}\rho_s\left((\dot{\mathbf{u}}_s^{+})^{\mathrm{T}}\dot{\mathbf{u}}_s^{+}+(\dot{\mathbf{u}}_s^{-})^{\mathrm{T}}\dot{\mathbf{u}}_s^{-}\right)\mathrm{d}\Omega_p,\quad \mathbf{u}_s^{\pm}=\left(U(z_\pm),\ V(z_\pm),\ W\right)^{\mathrm{T}} \tag{43}$$

In Eq. (43), ρ_s is the common surface mass density and the two velocity vectors are obtained by evaluating Eq. (9) at the external coordinates. Thus, the GM model contributes two stiffness energies and one surface kinetic energy, all expressed directly in terms of the same five generalized variables.

2.7 Interaction between the plate and ideal fluid

After the structural contributions have been established, the surrounding liquid is assumed inviscid, incompressible, and irrotational. The interaction between the plate and fluid is imposed by equating the normal velocity of the wetted plate surface to the fluid normal velocity, while the linearized fluid pressure provides the normal traction acting on the plate. The velocity potential, kinematic compatibility condition, and pressure relation are

$$\nabla^2\phi^{\alpha}=0,\qquad \frac{\partial\phi^{\alpha}}{\partial n}=\dot{w},\qquad p_f^{\alpha}=-\rho_f\dot{\phi}^{\alpha} \tag{44}$$

Here, ϕ^{α} is the potential in a fluid region, while p_f^{α} and ρ_f are the corresponding pressure and fluid density. For horizontal immersion, the plate motion is separated with the fundamental double sine mode

$$w(x,y,t)=q_f(t)\sin\left(\frac{\pi x}{a}\right)\sin\left(\frac{\pi y}{b}\right),\qquad \mu_f=\pi\sqrt{a^{-2}+b^{-2}} \tag{45}$$

The quantities $q_f(t)$ and μ_f are the modal amplitude and separation wavenumber. Applying the upper free surface condition, the lower rigid wall condition, and the compatibility condition in Eq. (44) gives

$$\phi^{+}=\frac{\dot{q}_f}{\mu_f}\frac{\sinh[\mu_f(z-h_1)]}{\cosh(\mu_f h_1)}\sin\left(\frac{\pi x}{a}\right)\sin\left(\frac{\pi y}{b}\right),\quad \phi^{-}=\frac{\dot{q}_f}{\mu_f}\frac{\cosh[\mu_f(z+h_2)]}{\sinh(\mu_f h_2)}\sin\left(\frac{\pi x}{a}\right)\sin\left(\frac{\pi y}{b}\right) \tag{46}$$

$$m_a^H=\frac{\rho_f}{\mu_f}\left[\tanh(\mu_f h_1)+\coth(\mu_f h_2)\right] \tag{47}$$

In Eqs. (46) and (47), h_1 and h_2 are the upper and lower fluid depths (Fig.1(a)) and m_a^H is the horizontal modal added mass per unit area. For vertical immersion, the same separation procedure is applied over the wet modal length, which gives

$$z_2^f=\min(h_{\mathrm{im}},b),\qquad \mu_f=\pi\sqrt{a^{-2}+(z_2^f)^{-2}},\qquad m_a^V=\frac{\rho_f}{\mu_f}\left[\coth(\mu_f d_1)+\coth(\mu_f d_2)\right] \tag{48}$$

Here, h_1 and h_2 are shown in Fig.1 (b), h_{im} is the immersed height and m_a^V is the corresponding vertical added mass per unit area. Both immersion models enter the formulation through the single fluid kinetic energy

$$T_f=\frac{1}{2}\int_{\Omega_p} m_a\,\dot{w}^2\,\mathrm{d}\Omega_p,\qquad m_a=\begin{cases} m_a^H, & \text{horizontal immersion,}\\ m_a^V, & \text{vertical immersion}\end{cases} \tag{49}$$

where m_a is the equivalent modal added mass per unit area for the prescribed immersion configuration. Eliminating the fluid potential condenses the plate-fluid interaction into an orientation-dependent added mass operator acting on the transverse plate motion. Consequently, under the adopted linear potential-flow assumptions, the ideal liquid modifies the generalized inertia but introduces no fluid stiffness or damping term.

The kinematic condition in Eq. (44) is imposed on the wetted surface of the physical fluid domain. After the fluid field has been eliminated, the equivalent modal coefficient in Eq. (49) is used over the full plate midsurface. For vertical partial immersion, the wetted length already enters Eq. (48), and no further wet area factor is introduced in the structural assembly.

2.8 Prescribed in-plane loading and governing equations

In the present dynamic stability problem, the plate is subjected to equal biaxial compression consisting of a static component and a harmonic component:

$$\mathbf{N}^0(t)=N(t)\mathbf{S}_B,\qquad N(t)=P_s+P_d\cos(\Omega t),\qquad \mathbf{S}_B=\begin{pmatrix}1&0\\0&1\end{pmatrix} \tag{50}$$

Here $N(t)$ is the common biaxial load, P_s and P_d are its static and dynamic amplitudes, Ω is the excitation frequency, and $\mathbf{S}_B$ defines the equal biaxial load pattern. With all structural and fluid energies now defined, Hamilton's principle reads

$$\delta\int_{t_1}^{t_2}\left[T_b+T_s+T_f-U_b-U_\mu-U_s-U_{zz}+W_g\right]\mathrm{d}t=0 \tag{51}$$

The quantities listed in Eq. (51), namely $T_b, T_s, T_f, U_b, U_\mu, U_s, U_{zz}$, and W_g, are the bulk, surface, and fluid kinetic energies; the bulk, MCST, surface, and normal stress energies; and the in plane load potential. The first variation of the latter is

$$\delta W_g=N(t)\int_{\Omega_p}(\delta\nabla w)^{\mathrm{T}}\mathbf{S}_B\nabla w\,\mathrm{d}\Omega_p \tag{52}$$

The generalized equilibrium equations can be written in terms of the following resultants. Let $\hat{\sigma}_i$ denote the in plane work stresses, with $i = x,y,xy$ identifying the two normal components and the shear component. The normal work stresses contain half the correction in Eqs. (39) and (40), while the remaining half enters through the variation of the Laplacian in Eq. (42):

$$\hat{\sigma}_{xx} = \sigma^b_{xx} + \tfrac{1}{2} c\nabla^2 w, \quad \hat{\sigma}_{yy} = \sigma^b_{yy} + \tfrac{1}{2} c\nabla^2 w, \quad \hat{\tau}_{xy} = \tau^b_{xy}. \tag{53}$$

$$D_{zz} = \tfrac{1}{2}\int_{-H/2}^{H/2} c(z)(\varepsilon_{xx} + \varepsilon_{yy})dz. \tag{54}$$

Use $\hat{\sigma}_i$ for the three quantities in Eq. (53), with $i = x, y, xy$, and $s_i^{\pm}$ for the corresponding incremental surface stress components in Eq. (36), excluding the constant residual stress. Let $[X]_{\pm}$ denote evaluation at $z = z_{\pm}$. Define

$$\mathcal{N}_i[g] = \int_{-H/2}^{H/2} g\hat{\sigma}_i dz + [g]_+ s_i^+ + [g]_- s_i^-. \tag{55}$$

$$N_i = \mathcal{N}_i[1], \qquad M_i = \mathcal{N}_i[z], \qquad F_i = \mathcal{N}_i[f]. \tag{56}$$

$$L_{ij}[g] = \int_{-H/2}^{H/2} g m_{ij} dz, \qquad S_i = \int_{-H/2}^{H/2} f' \tau^b_{iz} dz, \quad i = x, y. \tag{57}$$

$$\mathcal{I}_g(A) = \int_{-H/2}^{H/2} g\rho A dz + \rho_s([gA]_+ + [gA]_-). \tag{58}$$

In Eqs. (55)–(58), g is a thickness weight, N_i, M_i and F_i are the membrane, bending and higher order in plane resultants, L_{ij} is a weighted couple stress resultant, and S_i is a transverse shear resultant. The operator $\mathcal{I}_g$ weights a physical acceleration component A by bulk density and by the common exterior surface mass density ρ_s. The fluid part is kept outside $\mathcal{I}_g$ because it acts on w only.

The coefficients of the first derivatives of w in the spatial balance consist of rotary inertia, residual surface tension and applied compression. The coefficients of its second derivatives consist of the in plane moments, the reciprocal normal stress term, and the couple stress resultants:

$$A_x = -\mathcal{I}_z(\ddot{U}) + (2\tau_s - N(t))w_{,x}, \quad A_y = -\mathcal{I}_z(\ddot{V}) + (2\tau_s - N(t))w_{,y}. \tag{59}$$

$$H_{xx} = -M_x - L_{xy}[1] + D_{zz}, \quad H_{yy} = -M_y + L_{xy}[1] + D_{zz}. \tag{60}$$

$$2H_{xy} = -2M_{xy} + L_{xx}[1] - L_{yy}[1], \quad H_{yx} = H_{xy}. \tag{61}$$

For example, the factor of two in the mixed bending term follows from the coefficient of $w_{,xy}$ in Eq. (14), while D_{zz} multiplies each unmixed second derivative because it comes from the Laplacian. Taking the divergence of the first derivative work coefficients in Eq. (59) and the double divergence of the second derivative work coefficients in Eqs. (60) and (61) gives the transverse equation

$$\mathcal{I}_1(\ddot{w}) + m_a\ddot{w} - A_{x,x} - A_{y,y} + H_{xx,xx} + 2H_{xy,xy} + H_{yy,yy} = 0. \tag{62}$$

The corresponding in plane balances are

$$\mathcal{I}_1(\ddot{U}) - N_{x,x} - N_{xy,y} - \tfrac{1}{2}(L_{xz}[1])_{,xy} - \tfrac{1}{2}(L_{yz}[1])_{,yy} = 0. \tag{63}$$

$$\mathcal{I}_1(\ddot{V}) - N_{xy,x} - N_{y,y} + \tfrac{1}{2}(L_{xz}[1])_{,xx} + \tfrac{1}{2}(L_{yz}[1])_{,xy} = 0. \tag{64}$$

The first derivative work coefficients for the two rotations are denoted by $J_i^{(j)}$, where $j = x, y$ identifies the rotation and $i = x, y$ identifies the derivative direction:

$$J_x^{(x)} = F_x + \tfrac{1}{2} L_{xy}[f'], \quad J_y^{(x)} = F_{xy} + \tfrac{1}{2} L_{yy}[f']. \tag{65}$$

$$J_x^{(y)} = F_{xy} - \tfrac{1}{2} L_{xx}[f'], \quad J_y^{(y)} = F_y - \tfrac{1}{2} L_{xy}[f']. \tag{66}$$

Substituting Eqs. (65) and (66) gives the rotation balances

$$\mathcal{I}_f(\ddot{U}) + S_x + \tfrac{1}{2} L_{yz}[f''] - J_{x,x}^{(x)} - J_{y,y}^{(x)} - \tfrac{1}{2}(L_{xz}[f])_{,xy} - \tfrac{1}{2}(L_{yz}[f])_{,yy} = 0. \tag{67}$$

$$\mathcal{I}_f(\ddot{V}) + S_y - \tfrac{1}{2} L_{xz}[f''] - J_{x,x}^{(y)} - J_{y,y}^{(y)} + \tfrac{1}{2}(L_{xz}[f])_{,xx} + \tfrac{1}{2}(L_{yz}[f])_{,xy} = 0. \tag{68}$$

Equations (62)–(64), (67) and (68) are the transverse, two in plane and two rotation equations, respectively. In Eq. (62) the compressive load contributes $N(t)\nabla^2 w$, and the fluid contributes only $m_a \ddot{w}$. The essential conditions for the two restraints used in this work are given below.

(1) Simply supported

$$\begin{cases} (u, w, \theta_x)\big|_{y=0,b} = 0 \\ (v, w, \theta_y)\big|_{x=0,a} = 0 \end{cases} \tag{69}$$

(2) Fully clamped

$$\begin{cases} (u, v, w, \theta_x, \theta_y, w_{,y})\big|_{y=0,b} = 0 \\ (u, v, w, \theta_x, \theta_y, w_{,x})\big|_{x=0,a} = 0 \end{cases} \tag{70}$$

For CCCC edges, the zero normal slope of the transverse displacement is enforced by constraining the first interior control-point row.

For each generalized variable q, let A_i^q and H_{ij}^q denote the coefficients of the first and second derivatives of its virtual variation. They are obtained directly from the resultants above; the coefficient of a mixed derivative is divided equally between H_{xy}^q and H_{yx}^q. For an unloaded edge, the natural quantities obtained by integration by parts are

$$\mathcal{Q}_q = n_i(A_i^q - \partial_j H_{ij}^q) - \partial_s(n_i H_{ij}^q t_j). \tag{71}$$

$$\mathcal{M}_q = n_i H_{ij}^q n_j. \tag{72}$$

Here, n_i and t_i are the outward normal and the oriented tangent components, and ∂_s is the derivative along the edge. The quantity in Eq. (71) vanishes where the field value is free, and the quantity in Eq. (72) vanishes where the normal derivative is free. If the field value is free at a corner, the signed sum of the adjoining endpoint terms $n_i H_{ij}^q t_j$ vanishes. These natural conditions do not add prescribed control variables to the conditions above.

The corresponding weak equation is used for the isogeometric discretization in Section 3.

3. Isogeometric discretization and dynamic instability solution

Multiplying Eqs. (62)–(64), (67) and (68) by their respective admissible variations and integrating the derivative terms by parts gives the following weak equation. The edge and corner terms vanish under the conditions in Eqs. (69)–(72) and the associated corner conditions. This is also the result of substituting the energies and load work into Eq. (51), then integrating the kinetic terms by parts in time:

$$\mathcal{W}_b + \mathcal{W}_\mu + \mathcal{W}_s + \mathcal{W}_{zz} + \mathcal{W}_I - N(t)\mathcal{W}_g = 0 \tag{73}$$

The superscript η denotes a quantity evaluated from the admissible variation. The subscripts b, μ, s and zz identify the bulk, couple stress, direct surface and normal stress works. The last two terms describe inertia and the work of a unit biaxial compressive load, respectively.

The two normal surface strains $e_x^{\pm}$, $e_y^{\pm}$ and the engineering shear strain $\gamma^{\pm}$ are the components of Eq. (34). A plus or minus superscript denotes evaluation on the corresponding external surface.

$$\mathcal{W}_b = \int_{\Omega_p} \int_{-H/2}^{H/2} (\sigma_{xx}^b \varepsilon_{xx}^\eta + \sigma_{yy}^b \varepsilon_{yy}^\eta + \tau_{xy}^b \gamma_{xy}^\eta + \tau_{xz}^b \gamma_{xz}^\eta + \tau_{yz}^b \gamma_{yz}^\eta) dz d\Omega_p. \tag{74}$$

$$\mathcal{W}_{\mu}=\int_{\Omega_p}\int_{-H/2}^{H/2}(m_{xx}\chi_{xx}^{\eta}+m_{yy}\chi_{yy}^{\eta}+2m_{xy}\chi_{xy}^{\eta}+2m_{xz}\chi_{xz}^{\eta}+2m_{yz}\chi_{yz}^{\eta})dzd\Omega_p. \tag{75}$$

The two exterior membranes give the in plane surface work and the residual tension slope work in Eq. (76). In the normal stress work in Eq. (77), the two terms arise by varying the two factors of Eq. (42), respectively:

$$\mathcal{W}_s=\int_{\Omega_p}\sum_{\pm}(s_x^{\pm}e_x^{\eta,\pm}+s_y^{\pm}e_y^{\eta,\pm}+s_{xy}^{\pm}\gamma^{\eta,\pm}+\tau_s\nabla w\cdot\nabla w^{\eta})d\Omega_p. \tag{76}$$

$$\mathcal{W}_{zz}=\tfrac{1}{2}\int_{\Omega_p}\int_{-H/2}^{H/2}c[(\varepsilon_{xx}^{\eta}+\varepsilon_{yy}^{\eta})\nabla^2 w+(\varepsilon_{xx}+\varepsilon_{yy})\nabla^2 w^{\eta}]dzd\Omega_p. \tag{77}$$

The inertial work is obtained by one integration by parts in time of the bulk and surface velocity work and of the equivalent fluid kinetic energy. With $\mathbf{u}=(U,V,W)^T$ and $\mathbf{u}^{\eta}=(U^{\eta},V^{\eta},W^{\eta})^T$ denoting physical displacement and variation,

$$\mathcal{W}_I^b=\int_{\Omega_p}\int_{-H/2}^{H/2}\rho\ddot{\mathbf{u}}\cdot\mathbf{u}^{\eta}\,dzd\Omega_p. \tag{78}$$

$$\mathcal{W}_I^s=\int_{\Omega_p}\rho_s(\ddot{\mathbf{u}}^{+}\cdot\mathbf{u}^{\eta,+}+\ddot{\mathbf{u}}^{-}\cdot\mathbf{u}^{\eta,-})d\Omega_p,\quad \mathcal{W}_I^f=\int_{\Omega_p}m_a\ddot{w}w^{\eta}\,d\Omega_p \tag{79}$$

$$\mathcal{W}_I=\mathcal{W}_I^b+\mathcal{W}_I^s+\mathcal{W}_I^f,\quad \mathcal{W}_g=\int_{\Omega_p}\nabla w\cdot\nabla w^{\eta}\,d\Omega_p. \tag{80}$$

3.1 NURBS basis and generalized field approximation

In the framework of IGA [36], the continuous fields are discretized by the NURBS basis functions. The univariate B-spline basis is generated by the Cox-de Boor recursion

$$N_{i,0}(\xi)=\begin{cases}1, & \xi_i\le\xi<\xi_{i+1},\\ 0, & \text{otherwise}\end{cases},\quad N_{i,p}(\xi)=\frac{\xi-\xi_i}{\xi_{i+p}-\xi_i}N_{i,p-1}(\xi)+\frac{\xi_{i+p+1}-\xi}{\xi_{i+p+1}-\xi_{i+1}}N_{i+1,p-1}(\xi) \tag{81}$$

In Eq. (81), ξ and η are parametric coordinates and $N_{i,p}$ is a B-spline basis function of the specified degree. The tensor product rational basis is

$$R_A(\xi,\eta)=\frac{N_{i,p}(\xi)M_{j,q}(\eta)\omega_{ij}}{\sum_{k=1}^{n_c}\sum_{l=1}^{m_c}N_{k,p}(\xi)M_{l,q}(\eta)\omega_{kl}} \tag{82}$$

The symbol R_A denotes the two-dimensional NURBS basis associated with one control point. The exact geometry and the five generalized variables are interpolated as

$$\mathbf{x}^h(\xi,\eta)=\sum_A R_A\mathbf{P}_A,\qquad \mathbf{d}^h(\xi,\eta,t)=\sum_A R_A\mathbf{d}_A(t) \tag{83}$$

Here, $\mathbf{P}_A$ is a geometric control point and $\mathbf{d}_A$ contains its five generalized degrees of freedom. The same basis is therefore used for geometry and analysis.

3.2 Stiffness, mass and geometric stiffness matrices

Substituting the discrete displacement field from Eq. (83) into the weak form of Hamilton's principle, Eq. (73), and collecting the coefficients of the virtual degrees of freedom give the following equation of motion:

$$\mathbf{M}\ddot{\mathbf{q}}+\left[\mathbf{K}_0-\left(P_s+P_d\cos\Omega t\right)\mathbf{K}_g\right]\mathbf{q}=\mathbf{0} \tag{84}$$

Here, $\mathbf{q}$ is the vector of free generalized coordinates after the essential boundary conditions are imposed. $\mathbf{K}_0$, $\mathbf{M}$, and $\mathbf{K}_g$ are the global structural stiffness, total mass, and geometric stiffness matrices, respectively.

The stiffness and mass matrices are written as

$$\mathbf{K}_0 = \mathbf{K}_b + \mathbf{K}_\mu + \mathbf{K}_{zz} + \mathbf{K}_s, \qquad \mathbf{M} = \mathbf{M}_b + \mathbf{M}_s + \mathbf{M}_f \tag{85}$$

Here the stiffness matrices of the bulk $\mathbf{K}_b$, MCST $\mathbf{K}_\mu$, surface $\mathbf{K}_s$, and normal stress $\mathbf{K}_{zz}$ follow from the corresponding virtual work terms in Eqs. (74)–(77) and are expressed as:

$$\mathbf{K}_b = \int_{\Omega_p} \left(\begin{pmatrix} \mathbf{B}_1 \\ \mathbf{B}_2 \\ \mathbf{B}_3 \end{pmatrix}^{\mathrm{T}} \begin{pmatrix} \mathbf{C}_{11} & \mathbf{C}_{12} & \mathbf{C}_{13} \\ \mathbf{C}_{12} & \mathbf{C}_{22} & \mathbf{C}_{23} \\ \mathbf{C}_{13} & \mathbf{C}_{23} & \mathbf{C}_{33} \end{pmatrix} \begin{pmatrix} \mathbf{B}_1 \\ \mathbf{B}_2 \\ \mathbf{B}_3 \end{pmatrix} + \mathbf{B}_s{}^{\mathrm{T}} \mathbf{C}_s \mathbf{B}_s \right) \mathrm{d}\Omega_p \tag{86}$$

$$\mathbf{K}_\mu = \int_{\Omega_p} \left(\begin{pmatrix} \mathbf{X}_{p1} \\ \mathbf{X}_{p2} \end{pmatrix}^{\mathrm{T}} \begin{pmatrix} \mathbf{D}_{p,11} & \mathbf{D}_{p,12} \\ \mathbf{D}_{p,12} & \mathbf{D}_{p,22} \end{pmatrix} \begin{pmatrix} \mathbf{X}_{p1} \\ \mathbf{X}_{p2} \end{pmatrix} + \begin{pmatrix} \mathbf{X}_{s1} \\ \mathbf{X}_{s2} \\ \mathbf{X}_{s3} \end{pmatrix}^{\mathrm{T}} \begin{pmatrix} \mathbf{D}_{s,11} & \mathbf{D}_{s,12} & \mathbf{D}_{s,13} \\ \mathbf{D}_{s,12} & \mathbf{D}_{s,22} & \mathbf{D}_{s,23} \\ \mathbf{D}_{s,13} & \mathbf{D}_{s,23} & \mathbf{D}_{s,33} \end{pmatrix} \begin{pmatrix} \mathbf{X}_{s1} \\ \mathbf{X}_{s2} \\ \mathbf{X}_{s3} \end{pmatrix} \right) \mathrm{d}\Omega_p \tag{87}$$

$$\mathbf{K}_s = \int_{\Omega_p} \left(\begin{pmatrix} \mathbf{B}_1 \\ \mathbf{B}_2 \\ \mathbf{B}_3 \end{pmatrix}^{\mathrm{T}} \begin{pmatrix} \mathbf{S}_{11} & \mathbf{S}_{12} & \mathbf{S}_{13} \\ \mathbf{S}_{12} & \mathbf{S}_{22} & \mathbf{S}_{23} \\ \mathbf{S}_{13} & \mathbf{S}_{23} & \mathbf{S}_{33} \end{pmatrix} \begin{pmatrix} \mathbf{B}_1 \\ \mathbf{B}_2 \\ \mathbf{B}_3 \end{pmatrix} + \begin{pmatrix} \mathbf{B}_1 \\ \mathbf{B}_2 \\ \mathbf{B}_3 \end{pmatrix}^{\mathrm{T}} \begin{pmatrix} \mathbf{T}_{11} & \mathbf{T}_{12} & \mathbf{T}_{13} \\ \mathbf{T}_{12} & \mathbf{T}_{22} & \mathbf{T}_{23} \\ \mathbf{T}_{13} & \mathbf{T}_{23} & \mathbf{T}_{33} \end{pmatrix} \begin{pmatrix} \mathbf{B}_1 \\ \mathbf{B}_2 \\ \mathbf{B}_3 \end{pmatrix} + \mathbf{B}_G{}^{\mathrm{T}} \left(\tau_s^+ \mathbf{I}_2 + \tau_s^- \mathbf{I}_2 \right) \mathbf{B}_G \right) \mathrm{d}\Omega_p \tag{88}$$

$$\mathbf{K}_{zz} = \int_{\Omega_p} \left(\left(\mathbf{B}_1^{\mathrm{T}} \mathbf{Q}_D + \mathbf{B}_2^{\mathrm{T}} \mathbf{Q}_E + \mathbf{B}_3^{\mathrm{T}} \mathbf{Q}_F \right) \mathbf{B}_4 \right) \mathrm{d}\Omega_p \tag{89}$$

where

$$\mathbf{B}_1 = \begin{pmatrix} R_{,x} & 0 & 0 & 0 & 0 \\ 0 & R_{,y} & 0 & 0 & 0 \\ R_{,y} & R_{,x} & 0 & 0 & 0 \end{pmatrix}, \quad \mathbf{B}_2 = \begin{pmatrix} 0 & 0 & -R_{,xx} & 0 & 0 \\ 0 & 0 & -R_{,yy} & 0 & 0 \\ 0 & 0 & -2R_{,xy} & 0 & 0 \end{pmatrix}, \quad \mathbf{B}_3 = \begin{pmatrix} 0 & 0 & 0 & R_{,x} & 0 \\ 0 & 0 & 0 & 0 & R_{,y} \\ 0 & 0 & 0 & R_{,y} & R_{,x} \end{pmatrix},$$
$$\mathbf{B}_s = \begin{pmatrix} 0 & 0 & 0 & R & 0 \\ 0 & 0 & 0 & 0 & R \end{pmatrix}, \quad \mathbf{B}_4 = \begin{pmatrix} 0 & 0 & R_{,xx} + R_{,yy} & 0 & 0 \\ 0 & 0 & R_{,xx} + R_{,yy} & 0 & 0 \\ 0 & 0 & 0 & 0 & 0 \end{pmatrix}, \quad \mathbf{B}_G = \begin{pmatrix} 0 & 0 & R_{,x} & 0 & 0 \\ 0 & 0 & R_{,y} & 0 & 0 \end{pmatrix} \tag{90}$$

$$\mathbf{X}_{p1} = \begin{pmatrix} 0 & 0 & R_{,xy} & 0 & 0 \\ 0 & 0 & -R_{,xy} & 0 & 0 \\ 0 & 0 & (R_{,yy} - R_{,xx})/2 & 0 & 0 \end{pmatrix}, \quad \mathbf{X}_{p2} = \begin{pmatrix} 0 & 0 & 0 & 0 & -R_{,x}/2 \\ 0 & 0 & 0 & R_{,y}/2 & 0 \\ 0 & 0 & 0 & R_{,x}/4 & -R_{,y}/4 \end{pmatrix},$$
$$\mathbf{X}_{s1} = \frac{1}{4}\begin{pmatrix} -R_{,xy} & R_{,xx} & 0 & 0 & 0 \\ -R_{,yy} & R_{,xy} & 0 & 0 & 0 \end{pmatrix}, \quad \mathbf{X}_{s2} = \frac{1}{4}\begin{pmatrix} 0 & 0 & 0 & -R_{,xy} & R_{,xx} \\ 0 & 0 & 0 & -R_{,yy} & R_{,xy} \end{pmatrix}, \quad \mathbf{X}_{s3} = \frac{1}{4}\begin{pmatrix} 0 & 0 & 0 & 0 & -R \\ 0 & 0 & 0 & R & 0 \end{pmatrix} \tag{91}$$

The integrals over the lower face sheet, FG-TPMS core, and upper face sheet are combined as

$$\mathcal{I}_z[\mathcal{G}] = \int_{-H/2}^{-h_c/2} \mathcal{G}(z)\mathrm{d}z + \int_{-h_c/2}^{h_c/2} \mathcal{G}(z)\mathrm{d}z + \int_{h_c/2}^{H/2} \mathcal{G}(z)\mathrm{d}z \tag{92}$$

Here, $\mathcal{I}_z[\cdot]$ denotes the sum of the lower face sheet, FG-TPMS core, and upper face sheet integrations. $\mathcal{G}(z)$ denotes a generic scalar or matrix-valued integrand. The integral is evaluated separately over the two face sheets and the core using the material properties of each layer. The constitutive resultants in Eqs. (86)–(89) are calculated by

$$\mathbf{C}_{ij} = \mathcal{I}_z\left[a_i(z)\mathbf{Q}(z)a_j(z) \right], \quad \mathbf{C}_s = \mathcal{I}_z\left([f'(z)]^2 \mathbf{Q}_s(z) \right), \quad (a_1,\, a_2,\, a_3) = (1,\, z,\, f(z)) \tag{93}$$

$$\mathbf{D}_{p,ij} = \mathcal{I}_z\left[g_i(z)\mathbf{Q}_{\mu p}(z)g_j(z)\right], \quad (g_1,\ g_2) = (1,\ f'(z)),$$
$$\mathbf{D}_{s,ij} = \mathcal{I}_z\left[h_i(z)\mathbf{Q}_{\mu s}(z)h_j(z)\right], \quad (h_1,\ h_2,\ h_3) = (1,\ f(z),\ f''(z)) \tag{94}$$

$$\mathbf{Q}_D = \mathcal{I}_z[\mathbf{Q}_z(z)], \qquad \mathbf{Q}_E = \mathcal{I}_z[z\mathbf{Q}_z(z)], \qquad \mathbf{Q}_F = \mathcal{I}_z[f(z)\mathbf{Q}_z(z)] \tag{95}$$

$$\mathbf{S}_{ij} = a_i(z_+)\mathbf{D}_s a_j(z_+), \qquad \mathbf{T}_{ij} = a_i(z_-)\mathbf{D}_s a_j(z_-), \qquad i,j = 1,2,3 \tag{96}$$

The mass matrices of the bulk $\mathbf{M}_b$ and surfaces $\mathbf{M}_s$ in Eq. (85) follow from the bulk and surface inertial terms in Eqs. (78) and (79):

$$\mathbf{M}_b + \mathbf{M}_s = \int_{\Omega_p} \begin{pmatrix} \mathbf{M}_1 \\ \mathbf{M}_2 \\ \mathbf{M}_3 \end{pmatrix}^{\mathrm{T}} \left(\begin{pmatrix} \mathbf{Z}_{11} & \mathbf{Z}_{12} & \mathbf{Z}_{13} \\ \mathbf{Z}_{12} & \mathbf{Z}_{22} & \mathbf{Z}_{23} \\ \mathbf{Z}_{13} & \mathbf{Z}_{23} & \mathbf{Z}_{33} \end{pmatrix} + \begin{pmatrix} \mathbf{M}_{11}^{\pm} & \mathbf{M}_{12}^{\pm} & \mathbf{M}_{13}^{\pm} \\ \mathbf{M}_{12}^{\pm} & \mathbf{M}_{22}^{\pm} & \mathbf{M}_{23}^{\pm} \\ \mathbf{M}_{13}^{\pm} & \mathbf{M}_{23}^{\pm} & \mathbf{M}_{33}^{\pm} \end{pmatrix} \right) \begin{pmatrix} \mathbf{M}_1 \\ \mathbf{M}_2 \\ \mathbf{M}_3 \end{pmatrix} \mathrm{d}\Omega_p \tag{97}$$

$$\mathbf{M}_1 = \begin{pmatrix} R & 0 & 0 & 0 & 0 \\ 0 & R & 0 & 0 & 0 \\ 0 & 0 & R & 0 & 0 \end{pmatrix}, \ \mathbf{M}_2 = \begin{pmatrix} 0 & 0 & -R_{,x} & 0 & 0 \\ 0 & 0 & -R_{,y} & 0 & 0 \\ 0 & 0 & 0 & 0 & 0 \end{pmatrix}, \ \mathbf{M}_3 = \begin{pmatrix} 0 & 0 & 0 & R & 0 \\ 0 & 0 & 0 & 0 & R \\ 0 & 0 & 0 & 0 & 0 \end{pmatrix} \tag{98}$$

$$\mathbf{Z}_{ij} = \mathcal{I}_z\left[\rho(z)a_i(z)a_j(z)\mathbf{I}_3\right], \ \mathbf{M}_{ij}^{\pm} = \rho_s a_i(z_\pm)a_j(z_\pm)\mathbf{I}_3, \ i,j = 1,2,3 \tag{99}$$

The fluid mass matrix $\mathbf{M}_f$ follows from the transverse inertial term in Eq. (79):

$$\mathbf{M}_f = \int_{\Omega_p} m_a \mathbf{B}_f^{\mathrm{T}}\mathbf{B}_f \,\mathrm{d}\Omega_p, \qquad \mathbf{B}_f = [0 \quad 0 \quad R \quad 0 \quad 0] \tag{100}$$

Finally, the geometric stiffness matrix for the equal biaxial load follows from the unit load work in Eq. (80):

$$\mathbf{K}_g = \int_{\Omega_p} \mathbf{B}_G^{\mathrm{T}}\mathbf{S}_B\mathbf{B}_G \,\mathrm{d}\Omega_p \tag{101}$$

3.3 Principal instability boundaries

For the first principal instability region, the response is approximated by the following period-doubled sine and cosine trial functions:

$$\mathbf{q}_s(t) = \boldsymbol{\varphi}_s \sin\left(\frac{\Omega t}{2}\right), \qquad \mathbf{q}_c(t) = \boldsymbol{\varphi}_c \cos\left(\frac{\Omega t}{2}\right) \tag{102}$$

The vectors $\boldsymbol{\varphi}_s$ and $\boldsymbol{\varphi}_c$ are the modal amplitudes of the two branches. Substitution of Eq. (102) into Eq. (84), followed by harmonic balance of the fundamental terms at half the excitation frequency, gives

$$\left(\mathbf{K}_0 - \left(P_s - \frac{P_d}{2}\right)\mathbf{K}_g\right)\boldsymbol{\varphi}_s = \left(\frac{\Omega_s}{2}\right)^2 \mathbf{M}\boldsymbol{\varphi}_s \tag{103}$$

$$\left(\mathbf{K}_0 - \left(P_s + \frac{P_d}{2}\right)\mathbf{K}_g\right)\boldsymbol{\varphi}_c = \left(\frac{\Omega_c}{2}\right)^2 \mathbf{M}\boldsymbol{\varphi}_c \tag{104}$$

The two candidate frequencies Ω_s and Ω_c are obtained from Eqs. (103) and (104). The associated static buckling problem, normalized load amplitudes, and ordered instability boundaries are

$$\mathbf{K}_0\boldsymbol{\varphi}_b = P_{\mathrm{cr}}\mathbf{K}_g\boldsymbol{\varphi}_b, \ P_s = \gamma_s P_{\mathrm{cr}}, \ P_d = \gamma_d P_{\mathrm{cr}}, \ \Omega_L = \min(\Omega_s,\Omega_c), \ \Omega_U = \max(\Omega_s,\Omega_c) \tag{105}$$

Here P_{cr} is the static critical load, while Ω_L and Ω_U are the lower and upper boundaries of the first principal instability region. Equation (105) is the final dynamic instability region (DIR) output used for the convergence study and the parametric results on dynamic instability. It should be mentioned that only the fundamental terms of the period doubled trial solution are retained in Eqs. (103)–(105). The resulting boundaries are a first harmonic approximation to the principal instability region. Higher temporal harmonics are omitted, so the approximation is most reliable at small periodic load amplitudes. Quantitative stability limits at larger amplitudes require an analysis that retains those harmonics.

4. Numerical implementation and verification

This section presents the numerical settings, examines mesh convergence, and verifies the component formulations against published benchmark solutions. The SSSS and CCCC restraints are imposed as described in Section 2.8.

4.1 Numerical settings

Table 3 lists the geometry, material properties, immersion and loading parameters used for the convergence and parametric studies. Unless specified otherwise, these values are used throughout Section 5.

Table 3: Input parameters.

Group	Input
Geometry	$a=b=20\ \mu\mathrm{m}$; $H=1\ \mu\mathrm{m}$; $h_f/H=0.1$; $h_c/H=0.8$
Bulk materials (Al) and face grading (Al-Si)	$E_{\mathrm{Al}}=90$ GPa, $\nu_{\mathrm{Al}}=0.23$, $\rho_{\mathrm{Al}}=2700$ kg/m³; $E_{\mathrm{Si}}=210$ GPa, $\nu_{\mathrm{Si}}=0.24$, $\rho_{\mathrm{Si}}=2331$ kg/m³; $p_f=1$
Length scale parameter	$l/H=0,0.2,0.4,0.6$
GM constants of the silicon outer faces [37]	$\mu_s=-2.774$ N/m, $\lambda_s=-4.488$ N/m, $\tau_s=0.605$ N/m, $\rho_s=3.17\times10^{-7}$ kg/m²
Fluid density	$\rho_f=1000\ kg/m^3$
Horizontal immersion	$h_1/a=10$; $h_2/a=10$
Vertical immersion	$z_2/b=0.25$; $d_1/a=10$; $d_2/a=10$
Loading and DIR parameters	Load path: Equal biaxial; $\gamma_s=0.2$; $\gamma_d=0.5$
Nondimensionalization	$\bar{\Omega}=\Omega a^2/H\sqrt{\rho_{\mathrm{Al}}(1-\nu_{\mathrm{Al}}^2)/E_{\mathrm{Al}}}$; $\bar{P}_{cr}=P_{cr}a^2/D_{\mathrm{Al}}$; $D_{\mathrm{Al}}=E_{\mathrm{Al}}H^3/[12(1-\nu_{\mathrm{Al}}^2)]$

4.2 Convergence study

First, the convergence study is presented. Table 4 reports mesh convergence for the Al-Si graded sandwich with an Al TPMS core under SSSS restraint in both immersion configurations. The inputs follow Table 3 with both GM and MCST active, a length scale parameter of 0.2, and static and dynamic load factors of 0.2 and 0.5. Cubic NURBS, four Gauss points per in plane direction per element, and 30 thickness points in each layer are used. The maximum relative difference between the 11 × 11 and 13 × 13 meshes is below 0.001%. Therefore, The 11 × 11 mesh is retained in the subsequent analysis.

Table 4: Mesh convergence of the nondimensional buckling load and first harmonic instability boundaries.

Case	Elements	Buckling load	Lower boundary	Upper boundary
Horizontal immersion	5 × 5	20.7656	4.4451	6.1418
	7 × 7	20.7637	4.4449	6.1416
	9 × 9	20.7633	4.4449	6.1415
	11 × 11	20.7632	4.4449	6.1415
	13 × 13	20.7631	4.4449	6.1415
Vertical immersion	5 × 5	20.7656	6.8269	9.4327
	7 × 7	20.7637	6.8266	9.4323
	9 × 9	20.7633	6.8265	9.4322
	11 × 11	20.7632	6.8265	9.4322
	13 × 13	20.7631	6.8265	9.4321

4.3 Verification of TPMS homogenization and sandwich assembly

Table 5 compares the fundamental frequencies of simply supported and clamped FG-TPMS plates with the isogeometric results of Phung-Van et al. [18]. Excllent agreement can be seen. This comparison checks the effective core properties and the vibration solution.

Table 6 compares the critical loads of two FGM sandwich plates with the HSDT Navier solutions of El Meiche et al. [5] and the deep energy results of Shi et al. [6]. The latter used normalised hard constraints to impose the boundary conditions. The largest difference from the Navier solution is less than 0.1%.

Table 5: Comparison of dimensionless natural frequencies of FG-TPMS plates with the IWP topology, BB3 distribution, and different boundary conditions.

BC	Reference [18]	Present
SSSS	4.1442	4.1454
CCCC	5.2388	5.2630

Table 6: Comparison of nondimensional biaxial critical buckling loads of simply supported FGM sandwich plates.

Scheme	Power law index	HSDT Navier [5]	HSDT DEM [6]	Present
1-1-1	0.5	4.2182	4.2215	4.2183
	1	3.2323	3.2355	3.2324
	5	1.7894	1.7919	1.7898
	10	1.5969	1.5994	1.5974
1-2-1	0.5	4.6088	4.6116	4.6085
	1	3.7536	3.7563	3.7533
	5	2.3673	2.3697	2.3674
	10	2.1398	2.1422	2.1400

4.4 Verification of plates submerged in fluid

Table 7: Comparison of dimensionless natural frequencies of horizontally submerged isotropic plates for different h_1/a under SSSS and CCCC boundary conditions.

BC	Vac. Ref. [7]	Vac. present	h_1/a	Fluid Ref. [7]	Fluid present
SSSS	19.7390	19.7321	0.1	8.7730	8.7696
			0.5	7.6440	7.6421
			2	7.6060	7.6041
CCCC	36.1070	35.9465	0.1	16.0470	15.9760
			0.5	13.9830	13.9220
			2	13.9140	13.8529

Table 7 compares the vibration frequencies for horizontal immersion with the perturbation solutions of Soni et al. [7]. The frequency decreases as the fluid depth increases and changes little in the deep fluid range. The calculated values agree closely with the reference results for both SSSS and CCCC restraint.

Table 8 verifies the added mass formulation for vertical partial immersion. The comparison data come from Pham et al. [10], who used a refined higher order shear deformation theory with isogeometric analysis for plates in a fluid medium. The present results reproduce the decrease in frequency as the wetted height increases for all three length to thickness ratios. Together with Table 7, this comparison verifies the added mass calculation for both immersion directions. The GM surface module is examined next.

4.5 Verification of GM surface contributions

Table 9 compares the natural frequencies of nanoplates with surface effects with those obtained by Malekzadeh and Shojaee [22] using a two-variable first-order shear deformation theory. Table 10 compares the calculated buckling loads with the local limit of the plate model of Lu et al. [29], which includes surface effects and nonlocal strain gradient terms. In both Tables it can be observed that the differences are very small. Taken together, the core homogenisation, sandwich assembly, fluid added mass and surface terms are all verificatied in Tables 5-10.

Table 8: Comparison of dimensionless natural frequencies of vertically submerged isotropic plates for different z_2/b under the SSSS boundary condition.

a/H	Vac. Ref. [10]	Vac. present	z_2/b	Fluid Ref. [10]	Fluid present
5	1.7785	1.7683	0.1	1.7146	1.7017
			0.5	1.5354	1.5171
			1	1.4329	1.4126
10	1.9370	1.9317	0.1	1.7969	1.7903
			0.5	1.4735	1.4651
			1	1.3207	1.3121
100	2.0021	1.9993	0.1	1.2261	1.2243
			0.5	0.6871	0.6861
			1	0.5587	0.5578

Table 9: Comparison of dimensionless natural frequencies of an isotropic nanoplate including surface effects.

a/H	Reference [22]	Present
5	19.4378	19.3769
10	29.8757	29.8059
30	118.7195	118.6734
50	252.2362	252.2006

Table 10: Comparison of dimensionless critical buckling loads of an isotropic nanoplate including surface effects.

BC	Reference [29]	Present
SSSS	0.6269	0.6288
CCCC	0.7120	0.7144

4.6 Verification of the principal instability boundaries

Table 11 compares the first harmonic boundaries with the refined higher order shear deformation finite element results of Chakrabarti and Sheikh [38]. Their study gives the principal instability boundaries of a simply supported isotropic square plate under uniform uniaxial compression. For this comparison, the three layers are assigned identical homogeneous properties, and fluid inertia, GM surface effects and MCST are omitted. The plate has $a = b = 1\ \mathrm{m}$, $H = 0.01\ \mathrm{m}$ and $v = 0.3$. The material inputs are $E = 70\ \mathrm{GPa}$ and $\rho = 2700\ \mathrm{kg/m^3}$. The compression acts along the x direction only, with the static and dynamic load factors defined by Eq. (105) using the uniaxial critical load. The excitation frequency is reported on the reference scale $\bar{\Omega} = \Omega a^2 \sqrt{\rho H / D}$, where $D = EH^3 / \left[12(1-v^2)\right]$. The present boundaries agree with the published values for all six load combinations. This comparison verifies the computation of the first harmonic boundaries in the dry plate limit.

Table 11: Principal instability boundaries of the simply supported isotropic square plate under uniform uniaxial compression.

γ_s	γ_d	Reference $\bar{\Omega}_L$ [38]	Present $\bar{\Omega}_L$	Reference $\bar{\Omega}_U$ [38]	Present $\bar{\Omega}_U$
0.00	0.4	35.2920	35.2978	43.2240	43.2308
	0.8	30.5620	30.5688	46.6840	46.6945
0.20	0.4	30.5620	30.5688	39.4550	39.4641
	0.8	24.9530	24.9593	43.2210	43.2308
0.35	0.4	26.4690	26.4733	36.3790	36.3841
	0.8	19.7270	19.7320	40.4290	40.4387

5. Parametric studies and discussion

The following examples examine the critical buckling load and first principal instability region of the submerged sandwich plate. The surface and couple stress terms are compared first. The effects of immersion, thickness, preload and material grading are then examined.

5.1 Assessment of surface effects

Table 12 compares the nondimensional critical buckling load and principal instability boundaries with and without GM surface effects. Both boundary conditions and immersion orientations are considered at the four material length ratios in Table 3. Surface elasticity, residual stress, the normal stress correction and surface mass are switched on or off together. For the reference thickness, the inclusion of GM terms raises the critical load and both boundaries in all cases in Table 12. The increase is small compared with the changes obtained by varying the MCST length ratio. Clamped plates give higher loads and frequencies than simply supported plates.

The increases in Table 12 are the net result of the GM terms. The negative silicon surface elastic constants act together with the tensile residual surface stress, the normal stress correction and surface inertia. The immersion orientation changes the two dynamic boundaries but leaves the static load unchanged, since the ideal fluid enters only the mass matrix.

Table 12: Nondimensional critical buckling loads and principal instability boundaries with and without surface effects.

Immersion	BC	l/H	SE	$\bar{N}_{cr}$	$\bar{\Omega}_L$	$\bar{\Omega}_U$
Horizontal	SSSS	0.0	Off	18.4508	4.1903	5.7897
			On	18.5009	4.1958	5.7974
		0.2	Off	20.7136	4.4397	6.1343
			On	20.7632	4.4449	6.1415
		0.4	Off	26.2984	5.0025	6.9119
			On	26.3474	5.0070	6.9181
		0.6	Off	35.0293	5.7734	7.9771
			On	35.0781	5.7772	7.9824
	CCCC	0.0	Off	43.0317	7.1295	9.7367
			On	43.0696	7.1323	9.7405
		0.2	Off	50.9049	7.7912	10.6543
			On	50.9395	7.7935	10.6574
		0.4	Off	67.5696	9.0126	12.3402
			On	67.6010	9.0143	12.3425
		0.6	Off	91.5505	10.5077	14.3950
			On	91.5804	10.5091	14.3968
Vertical	SSSS	0.0	Off	18.4508	6.4359	8.8925
			On	18.5009	6.4442	8.9040
		0.2	Off	20.7136	6.8188	9.4216
			On	20.7632	6.8265	9.4322
		0.4	Off	26.2984	7.6830	10.6155
			On	26.3474	7.6896	10.6246
		0.6	Off	35.0293	8.8669	12.2514
			On	35.0781	8.8724	12.2590
	CCCC	0.0	Off	43.0317	10.9506	14.9554
			On	43.0696	10.9545	14.9606
		0.2	Off	50.9049	11.9660	16.3637
			On	50.9395	11.9690	16.3677
		0.4	Off	67.5696	13.8409	18.9515
			On	67.6010	13.8429	18.9542
		0.6	Off	91.5505	16.1365	22.1065
			On	91.5804	16.1378	22.1082

5.2 Effect of fluid immersion parameters

After the surface contribution has been identified, Fig. 2 examines how the first principal instability region changes with fluid immersion. All inputs follow Table 3 except the immersion parameters: the horizontal cases use $h_2/a=10$ with $h_1/a=0$, 0.2, and 1.0, whereas the vertical cases use $d_1/a=d_2/a=10$ with $z_2/b=0.1$, 0.5, and 1.0. As the horizontal fluid depth or the vertical wetted height increases, both instability boundaries move to lower frequencies (Fig. 2). The shift is greatest in shallow horizontal immersion and becomes small as the depth increases. The vertical curves remain separated over the selected wetted heights. Clamped restraint raises the frequency level without

changing these trends. It is because of that the downward shift follows from the increase in added mass as the fluid domain participating in the motion becomes larger.

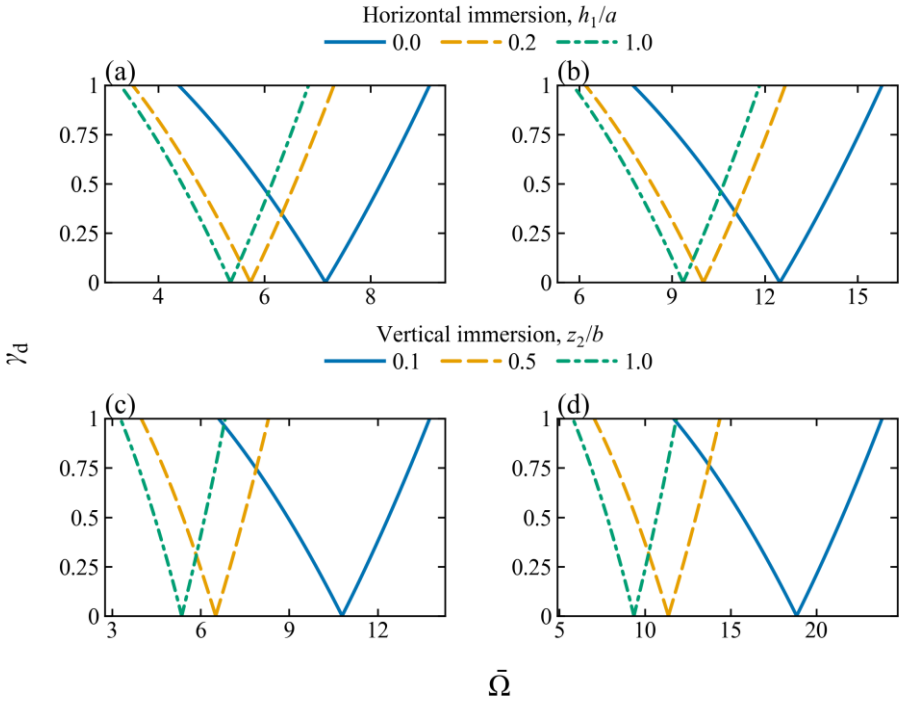


Fig 2: Principal instability regions of sandwich plates with an FG-TPMS core under different fluid immersion and boundary conditions: (a) horizontal immersion, SSSS; (b) horizontal immersion, CCCC; (c) vertical immersion, SSSS; and (d) vertical immersion, CCCC.

5.3 Effect of the MCST length scale parameter on the principal instability region

Figure 3 describes the influence of the MCST material length scale on the first principal instability region. Relative to Table 3, only l/H is varied; the GM surface model and all other structural, fluid, load, and numerical inputs remain unchanged. Fig. 3 (a) and (b) correspond to horizontal deep immersion with SSSS and CCCC boundaries, and (c) and (d) show the corresponding vertical partial immersion cases.

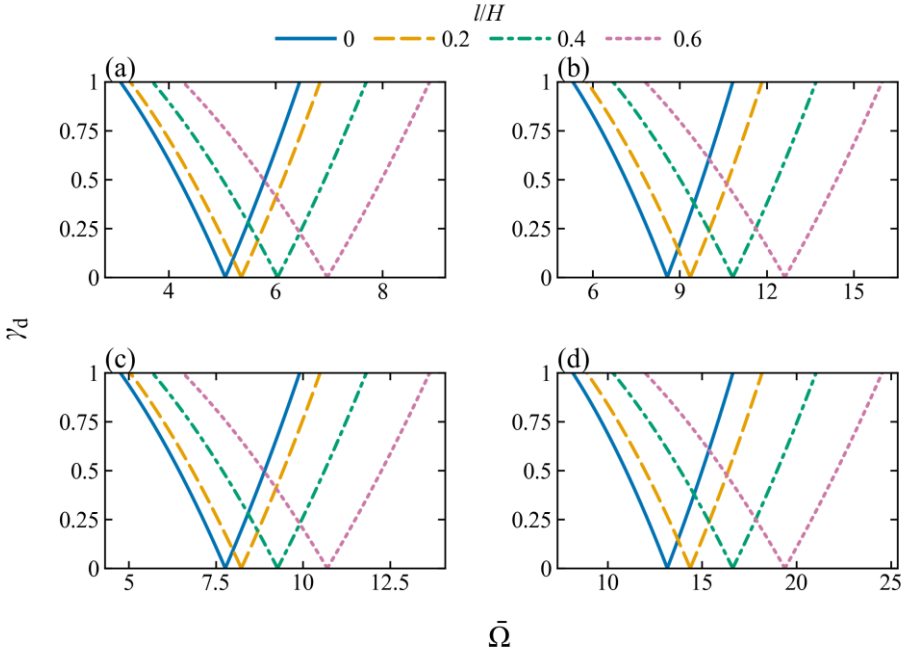


Fig 3: Effect of the MCST length scale parameter on the principal instability region of sandwich plates with an FG-TPMS core under different fluid immersion and boundary conditions: (a) horizontal deep immersion, SSSS; (b) horizontal deep immersion, CCCC; (c) vertical partial immersion, SSSS; and (d) vertical partial immersion, CCCC.

The lower and upper boundaries in Fig. 3 rise as the material length ratio increases, and the interval between them widens. The same trend is observed for both restraints and both immersion orientations. Additionally, increasing the length ratio increases the couple stress stiffness without changing the mass. The effect therefore becomes more important as the plate thickness decreases at a fixed material length.

5.4 Effect of plate thickness and its coupling with GM surface and MCST size effects

To examine how thickness controls the relative importance of the GM surface and MCST size effects, the static buckling load and first principal instability region are evaluated for six plate thicknesses. Unless stated otherwise, all inputs retain the values in Table 3. Throughout the sweep, $a=b=20H$ is maintained to preserve geometric similarity, and the MCST material length is fixed at $l=0.01\ \mu\text{m}$.

Four theoretical descriptions are evaluated at every thickness: the classical model, the GM surface model, the MCST model, and the combined GM and MCST model. The classical model omits both small scale corrections; the GM and MCST models activate the surface and couple stress contributions separately; and the combined model includes both. To isolate the thickness dependence of the structural corrections from a change in relative fluid inertia, the fluid depths and clearances are scaled with the in-plane dimensions. Thus, a/H and b/H, together with the ratio of fluid added mass to bulk plate mass, remain constant along the geometrically similar sequence.

Figure 4 shows the variation of critical buckling load with thickness. The difference between the MCST and classical predictions is largest for the thinnest plates. The horizontal and vertical results coincide at a given thickness because the added mass does not enter the buckling problem. Additionally, the clamped plate has the larger critical load.

Because a thickness change may translate the instability region and simultaneously alter its extent, the dynamic results are characterized by both the center and the width of the first principal instability region. Using the nondimensional lower and upper boundaries, these quantities are defined as

$$\Omega_c=\frac{\Omega_L+\Omega_U}{2},\qquad \Delta\Omega=\Omega_U-\Omega_L \tag{106}$$

where Ω_c is the arithmetic mean of the two boundaries and therefore locates the instability region on the excitation frequency axis. $\Delta\Omega$ is their difference and measures the width of the unstable interval; a larger value indicates that principal parametric instability can occur over a broader excitation frequency range.

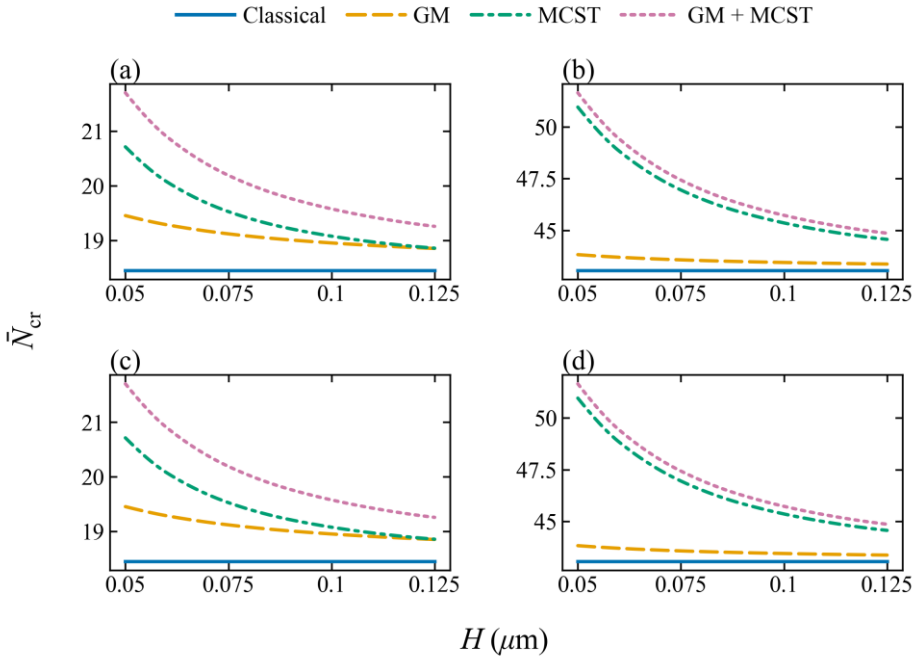


Fig 4: Thickness dependence of the nondimensional critical buckling load of sandwich plates with an FG-TPMS core under different fluid immersion and boundary conditions: (a) horizontal deep immersion, SSSS; (b) horizontal deep immersion, CCCC; (c) vertical partial immersion, SSSS; and (d) vertical partial immersion, CCCC.

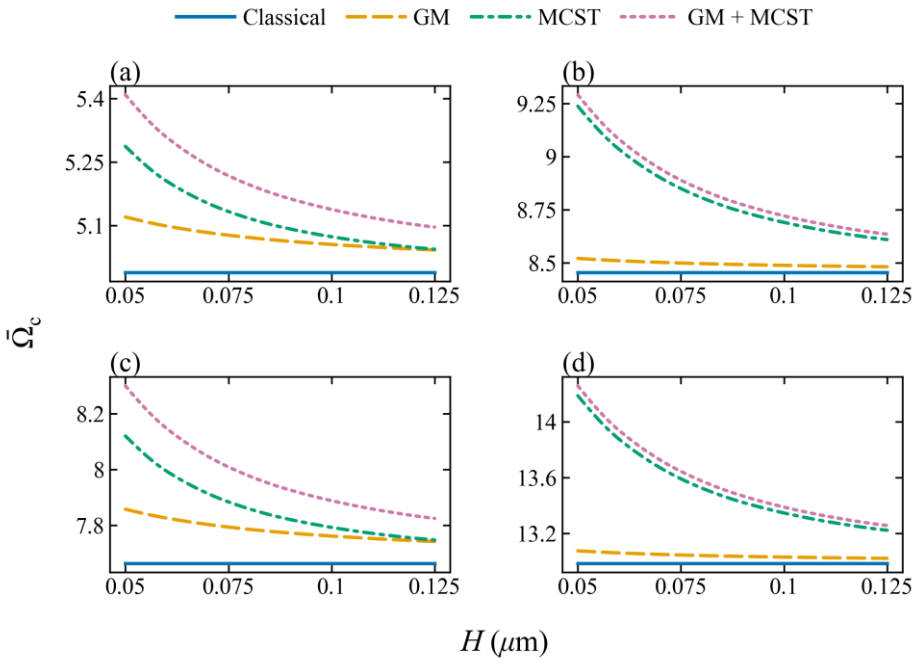


Fig 5: Thickness dependence of the center of the principal instability region for sandwich plates with an FG-TPMS core under different fluid immersion and boundary conditions: (a) horizontal deep immersion, SSSS; (b) horizontal deep immersion, CCCC; (c) vertical partial immersion, SSSS; and (d) vertical partial immersion, CCCC.

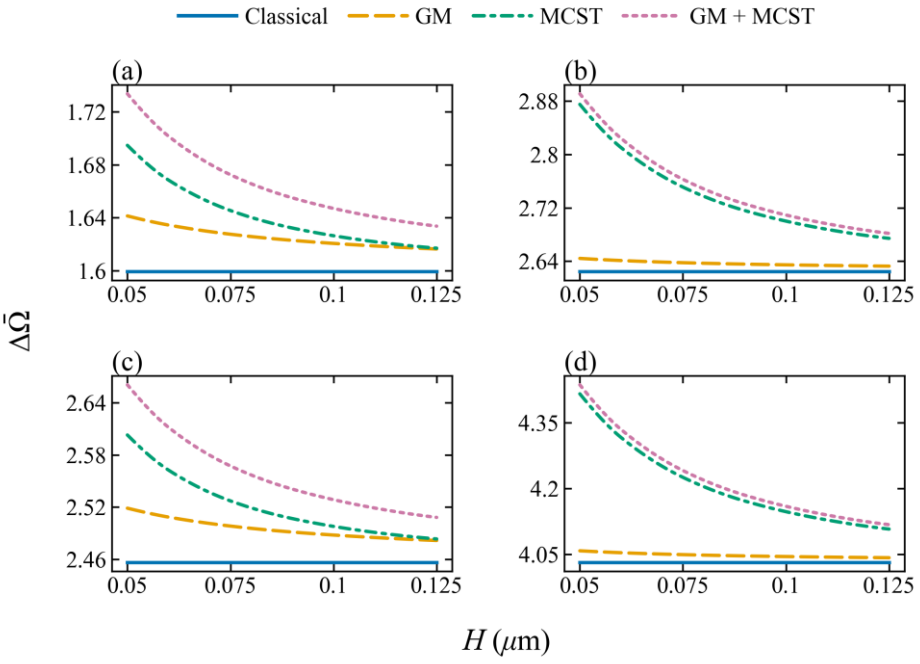


Fig 6: Thickness dependence of the width of the principal instability region for sandwich plates with an FG-TPMS core under different fluid immersion and boundary conditions: (a) horizontal deep immersion, SSSS; (b) horizontal deep immersion, CCCC; (c) vertical partial immersion, SSSS; and (d) vertical partial immersion, CCCC.

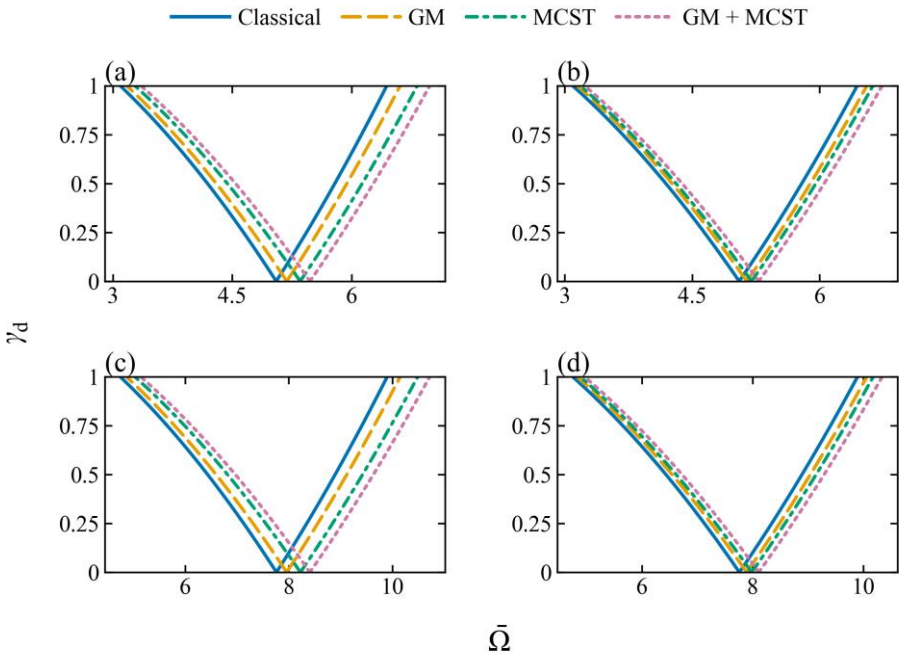


Fig 7: Principal instability regions of sandwich plates with an FG-TPMS core under different fluid immersion: (a) H = 0.05 μm under horizontal deep immersion; (b) H = 0.075 μm under horizontal deep immersion; (c) H = 0.05 μm under vertical partial immersion; and (d) H = 0.075 μm under vertical partial immersion. All cases use SSSS boundaries.

Figures 5 and 6 give the center and width of the instability region at a dynamic load factor of 0.5. The four models separate as the plate becomes thinner. For the same structural model, the center is higher in vertical partial immersion because the added mass is smaller than in horizontal deep immersion. Figure 7 shows that in both immersion orientations the instability boundaries draw closer as the plate thickens and the GM and MCST effects weaken.

5.5 Effect of the sandwich core thickness ratio

Figures 8-10 investigate the effect of the sandwich core thickness ratio on the complete instability region. Relative to Table 3, the total thickness is fixed and the core ratios are $h_c / H \in (0.5,\ 0.6,\ 0.7,\ 0.8,\ 0.9)$. For the symmetric sandwich, the thickness of each face sheet follows from $h_f / H = (1 - h_c / H)/2$, giving $h_f / H \in (0.25,\ 0.20,\ 0.15,\ 0.10,\ 0.05)$. Both immersion directions and both boundary conditions are included.

As shown in Fig. 8, increasing the core thickness ratio shifts both instability boundaries toward lower excitation frequencies. Clamping and vertical partial immersion give higher boundary frequencies than their respective counterparts, but neither changes the ordering of the curves with core thickness ratio.

Figures 9 and 10 distinguish a shift in the position of the instability region from a change in its width. At a given positive dynamic load factor, a larger core thickness ratio gives a lower center frequency and a narrower instability region. For a fixed core thickness ratio, increasing the dynamic load factor causes the two boundaries to separate from their common value at zero dynamic load. The width increases nearly linearly over the range shown, whereas the center frequency decreases only slightly. Thus, increasing the core thickness ratio shifts and narrows the instability region, while increasing the dynamic load factor mainly widens it.

The shift toward lower frequencies can be explained by the change in the distribution of stiffness through the thickness. At fixed total thickness, a thicker porous core replaces part of the stiffer Al-Si face sheets. The lost face sheet material is located away from the midplane, where it contributes strongly to bending stiffness. Although the structural mass also decreases, the lower center frequencies indicate that the reduction in effective stiffness dominates the change in inertia for the cases considered.

5.6 Effect of the static load factor

The first principal instability region as the static compressive load changes is examined in this example. All parameters follow Table 3 except the four static load factors $\gamma_s \in (0,\ 0.1,\ 0.2,\ 0.4)$. The reference sandwich distribution remains $h_c / H = 0.8$ and $h_f / H = 0.1$, and the harmonic factor varies over $\gamma_d = 0 : 0.1 : 1$. The largest

value $\gamma_s = 0.4$ is selected so that $\gamma_s + \gamma_d / 2 = 0.90 < 1$ throughout the sweep, thereby maintaining a positive first mode effective stiffness relative to the static critical state.

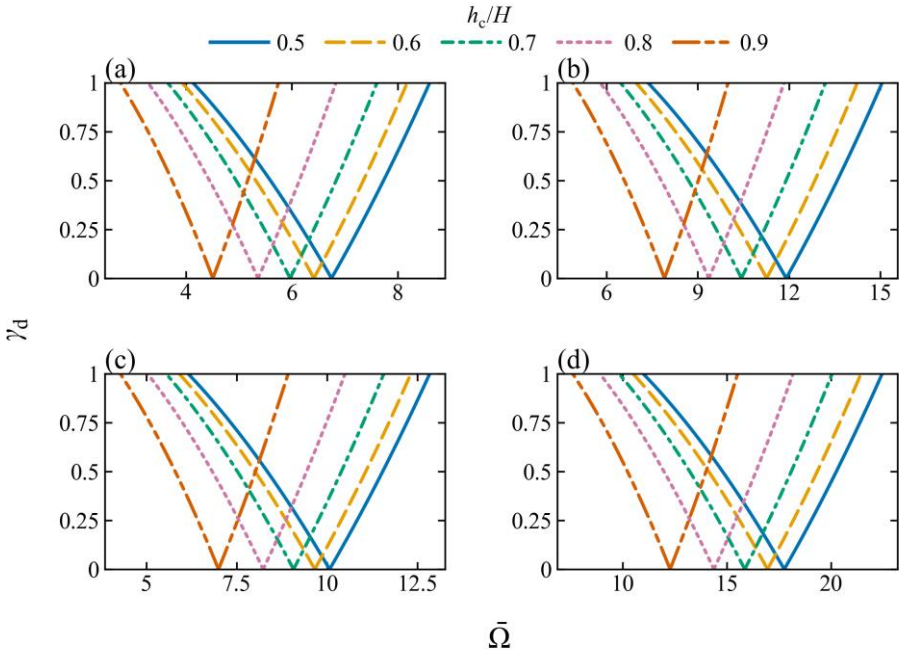


Fig 8: Principal instability regions for different core thickness ratios of sandwich plates with an FG-TPMS core under different fluid immersion and boundary conditions: (a) horizontal deep immersion, SSSS; (b) horizontal deep immersion, CCCC; (c) vertical partial immersion, SSSS; and (d) vertical partial immersion, CCCC. Legend values are the core thickness ratios.

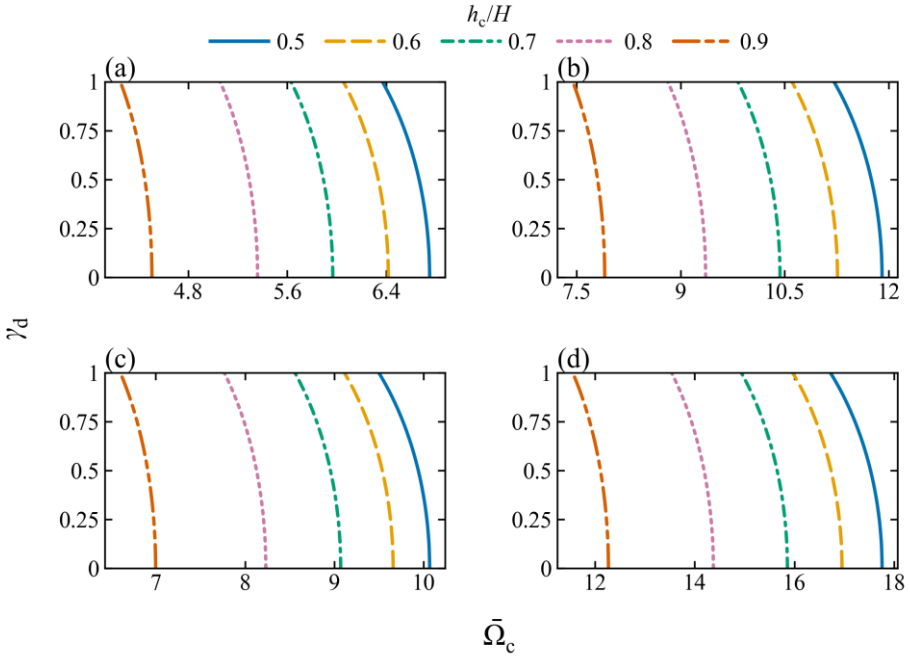


Fig 9: Evolution of the center of the principal instability region for different core thickness ratios of sandwich plates with an FG-TPMS core under different fluid immersion and boundary conditions: (a) horizontal deep immersion, SSSS; (b) horizontal deep immersion, CCCC; (c) vertical partial immersion, SSSS; and (d) vertical partial immersion, CCCC.

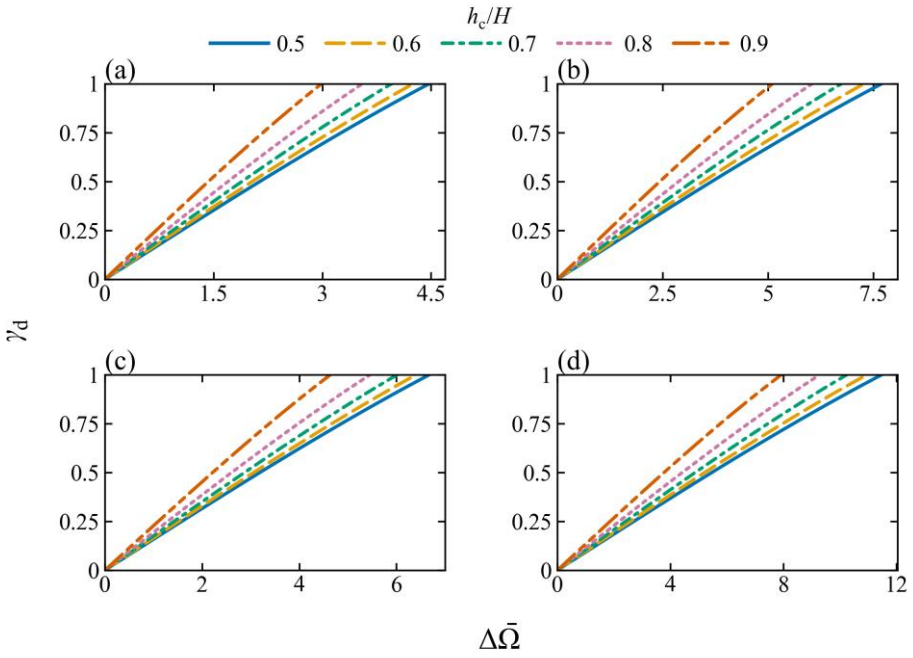


Fig 10: Evolution of the width of the principal instability region for different core thickness ratios of sandwich plates with an FG-TPMS core under different fluid immersion and boundary conditions: (a) horizontal deep immersion, SSSS; (b) horizontal deep immersion, CCCC; (c) vertical partial immersion, SSSS; and (d) vertical partial immersion, CCCC.

As the static load factor increases, the vertex and both boundaries in Fig. 11 move to lower frequencies. At the same dynamic load factor, the unstable interval is wider. Both trends hold for the two restraints and immersion orientations.

This behavior arises because the static compressive load reduces the effective stiffness of the plate before the harmonic component is applied. The reduced stiffness shifts the principal instability region to lower frequencies and makes the plate more sensitive to the harmonic load, resulting in a wider instability region at the same dynamic load factor.

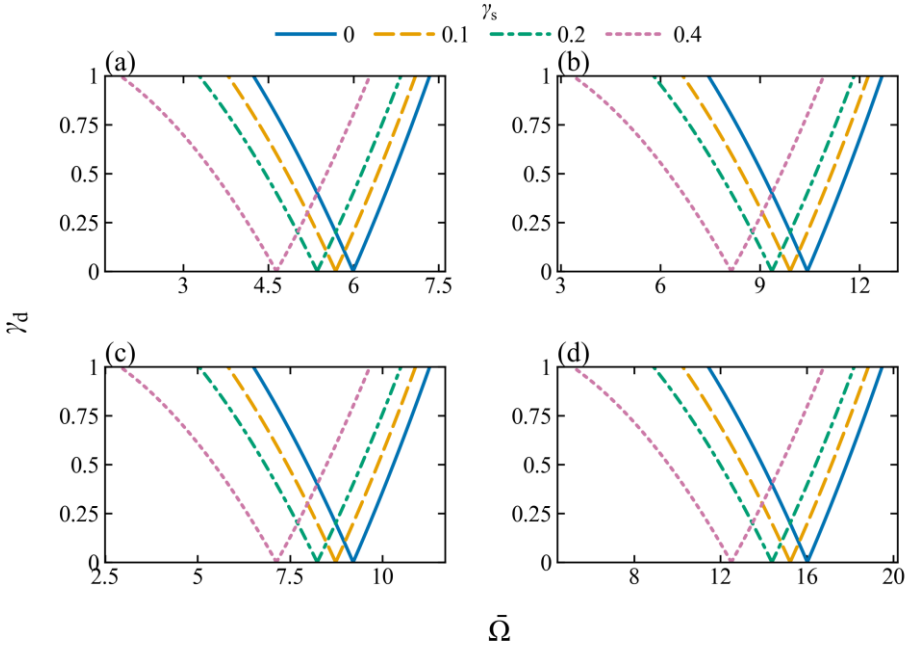


Fig 11: Effect of the static load factor on the principal instability region of sandwich plates with an FG-TPMS core under different fluid immersion and boundary conditions: (a) horizontal deep immersion, SSSS; (b) horizontal deep immersion, CCCC; (c) vertical partial immersion, SSSS; and (d) vertical partial immersion, CCCC.

5.7 Effect of face material grading

Figure 12 shows how the face gradient exponent affects the principal instability regions of simply supported plates under horizontal and vertical immersion. The dynamic load factor ranges from 0 to 1 in steps of 0.1. Both GM and MCST are included, and the material length to thickness ratio is 0.2. In both immersion configurations, increasing the face gradient exponent shifts the vertex and both instability boundaries toward lower excitation frequencies. At a given positive dynamic load factor, the two boundaries also move closer together. Vertical immersion gives higher boundary frequencies than horizontal immersion for the cases shown, but the ordering of the curves with the face gradient exponent is the same in both configurations.

The shift toward lower frequencies follows from the change in material composition within the face sheets. The adopted gradation gives a mean silicon volume fraction of $1/(1+p_f)$, so increasing exponent reduces the silicon content through the thickness of each face sheet while leaving its outermost surface pure silicon. The loss of silicon below the outer surface reduces the bending stiffness because the material in this region lies far from the plate midplane. Replacing silicon with aluminium also increases the structural mass for the material densities used here. Both changes favour a shift to lower frequencies.

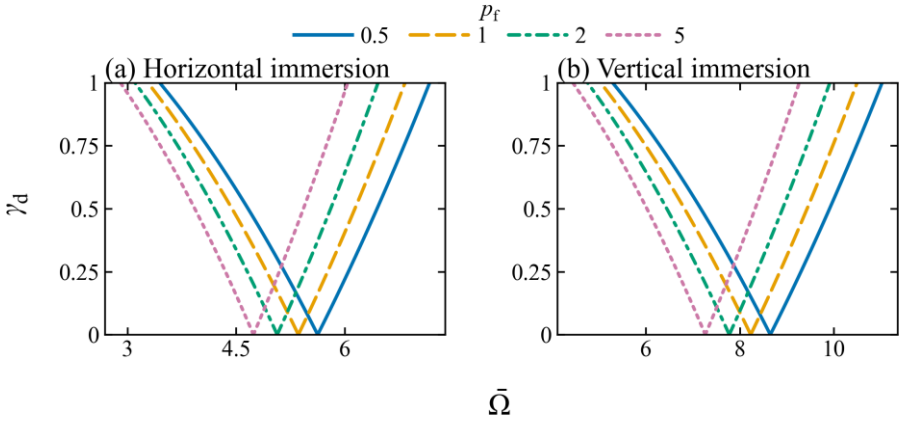


Fig 12: Effect of the face gradient exponent on the principal instability regions of simply supported sandwich plates under (a) horizontal and (b) vertical immersion. For each exponent, the left and right branches are the lower and upper boundaries, respectively.

5.8 Accuracy of the first harmonic approximation

Finally, Table 13 compares the first harmonic boundaries with a multi-harmonic solution. The plate is simply supported on all four edges and fully submerged horizontally. Both MCST and GM surface effects are retained. The static load factor is $\gamma_s = 0.2$, and only the dynamic load factor γ_d varies from 0.1 to 1.0. The two load factors are based on the same static buckling load in both methods, and the frequency normalization is that of Table 3.

The multi-harmonic solution extends the period-doubled trial functions of Eq. (102). First, the matrices of Eq. (84) are projected onto the mass-normalized vibration modes of the plate with the prescribed static compression and fluid added mass. In this modal basis, the period-doubled response is expanded as

$$\mathbf{q}(t) = \sum_{j=1}^{N_h} \left[\mathbf{a}_j \sin \frac{(2j-1)\Omega t}{2} + \mathbf{b}_j \cos \frac{(2j-1)\Omega t}{2} \right] \tag{107}$$

Here $\mathbf{q}$ denotes the reduced modal coordinates, $\mathbf{a}_j$ and $\mathbf{b}_j$ are the sine and cosine coefficient vectors, and N_h is the number of retained odd harmonics. Only odd orders are retained because the response at the principal period-doubling boundary reverses sign after one forcing period. Multiplication by the harmonic load couples adjacent odd orders. The sine and cosine series give separate generalized eigenproblems for the squared half excitation frequency. The principal branches are followed from the lowest loaded frequency at zero dynamic load.

The reference solution retains 48 spatial modes and nine odd harmonics, with orders 1, 3, 5, …, 17. Increasing the basis from 32 modes and seven odd harmonics (orders 1 through 13) changes either nondimensional boundary by less than 10^{-8} over the sweep. In Table 13, the percentage differences are absolute and are evaluated with respect to the multi-harmonic result.

For this configuration, the differences in both boundaries and in interval width are below 1.5% at the tested load factors up to $\gamma_d = 0.5$. As the dynamic load increases, the lower boundary becomes more sensitive to the omitted harmonics. The first harmonic approximation places both boundaries below the multi-harmonic values, but the shift is much larger on the lower side. The resulting interval is therefore too wide. At $\gamma_d = 1.0$, the lower boundary differs by 12.57%, whereas the upper boundary differs by less than 1%. For the configuration considered, the first harmonic approximation agrees closely with the multi-harmonic solution at small dynamic load amplitudes, but at larger amplitudes it should be used only to identify qualitative trends rather than to establish quantitative stability limits.

6. Conclusions

The static buckling and principal instability of a submerged sandwich plate with Al-Si graded faces and an FG-TPMS core were analysed. The calculations give the following results.

(1) The net GM contribution slightly increases the critical buckling load and both instability boundaries.
(2) Increasing the fluid domain lowers both instability boundaries through the increase in added mass. For the selected inputs, vertical partial immersion gives higher frequencies than horizontal deep immersion.
(3) The principal instability frequencies increase with the MCST length. At fixed material length, the MCST correction is more pronounced for thinner plates.
(4) At fixed total thickness, increasing the core ratio lowers the center and narrows the instability region. A higher static compressive load also lowers the center but widens the region.
(5) Increasing the face gradient exponent lowers both principal instability boundaries and narrows the instability region at a given positive dynamic load factor.

The conclusions apply to the selected parameters within a linear, homogenized continuum model. The MCST length and GM constants have not been calibrated for an actual FG-TPMS sandwich; internal pore surface effects, liquid penetration, viscosity, damping, and nonlinear motion after instability are excluded. Additionally, the first harmonic boundaries lose accuracy at large dynamic load amplitudes, for which higher temporal harmonics must be included before drawing quantitative design conclusions. Future work should combine cell resolved or experimental calibration with a more general fluid model and nonlinear stability analysis.

Table 13: First harmonic and multi-harmonic principal instability boundaries for the horizontally submerged SSSS sandwich plate.

	Lower boundary $\bar{\Omega}_L$			Upper boundary $\bar{\Omega}_U$		
γ_d	First	Multi	Diff. (%)	First	Multi	Diff. (%)
0.1	5.1906	5.1920	0.03	5.5258	5.5270	0.02
0.2	5.0146	5.0211	0.13	5.6860	5.6903	0.08
0.3	4.8322	4.8486	0.34	5.8418	5.8507	0.15
0.4	4.6426	4.6756	0.71	5.9935	6.0081	0.24
0.5	4.4449	4.5036	1.30	6.1416	6.1625	0.34
0.6	4.2381	4.3348	2.23	6.2861	6.3140	0.44
0.7	4.0206	4.1719	3.63	6.4274	6.4627	0.55
0.8	3.7907	4.0185	5.67	6.5656	6.6086	0.65
0.9	3.5458	3.8783	8.57	6.7010	6.7519	0.75
1.0	3.2828	3.7547	12.57	6.8337	6.8927	0.86

References

[1] N. V. Viet, W. Zaki, Free vibration and buckling characteristics of functionally graded beams with triply periodic minimal surface architecture, *Composite Structures,* Vol. 274, pp. 114342, 2021.
[2] H. Nguyen-Xuan, K. Q. Tran, C. H. Thai, J. Lee, Modelling of functionally graded triply periodic minimal surface (FG-TPMS) plates, *Composite Structures,* Vol. 315, pp. 116981, 2023.

[3] T. N. Nguyen, N. Wattanasakulpong, N. P. Nguyen, P. Fakharian, S. Eiadtrong, Isogeometric analysis of functionally graded triply periodic minimal surface shells, *Mechanics of Advanced Materials and Structures,* Vol. 32, No. 21, pp. 5447–5460, 2024.

[4] J. Feng, J. Fu, C. Shang, Z. Lin, B. Li, Sandwich panel design and performance optimization based on triply periodic minimal surfaces, *Computer-Aided Design,* Vol. 115, pp. 307–322, 2019.

[5] N. El Meiche, A. Tounsi, N. Ziane, I. Mechab, E. A. Adda.Bedia, A new hyperbolic shear deformation theory for buckling and vibration of functionally graded sandwich plate, *International Journal of Mechanical Sciences,* Vol. 53, No. 4, pp. 237–247, 2011.

[6] P. Shi, V. N. V. Hoang, J. Yang, X. Yang, R. Kiran, H. Shou, P. T. Thanh, A deep energy method with normalized hard constraints for mechanical buckling analysis of FGM sandwich plates using higher-order shear deformation theory, *Composite Structures,* Vol. 393, pp. 120586, 2026.

[7] S. Soni, N. K. Jain, P. V. Joshi, Vibration analysis of partially cracked plate submerged in fluid, *Journal of Sound and Vibration,* Vol. 412, pp. 28–57, 2018.

[8] M. E. Yildizdag, I. T. Ardic, M. Demirtas, A. Ergin, Hydroelastic vibration analysis of plates partially submerged in fluid with an isogeometric FE-BE approach, *Ocean Engineering,* Vol. 172, pp. 316–329, 2019.

[9] A. Ramian, R. A. Jafari-Talookolaei, P. S. Valvo, M. Abedi, Free vibration analysis of sandwich plates with compressible core in contact with fluid, *Thin-Walled Structures,* Vol. 157, pp. 107088, 2020.

[10] Q. H. Pham, P. C. Nguyen, V. K. Tran, T. Nguyen-Thoi, Isogeometric analysis for free vibration of bidirectional functionally graded plates in the fluid medium, *Defence Technology,* Vol. 18, No. 8, pp. 1311–1329, 2022.

[11] W. Chen, P. Xiang, P. Shi, Z. Liu, B. Deng, Higher-order isogeometric thermal vibration analysis of functionally graded porous microplates interacting with an ideal fluid, *Case Studies in Thermal Engineering,* Vol. 76, pp. 107431, 2025.

[12] F. Yang, A. C. M. Chong, D. C. C. Lam, P. Tong, Couplestress based strain gradient theory for elasticity, *International Journal of Solids and Structures,* Vol. 39, No. 10, pp. 2731–2743, 2002.

[13] J. Kim, K. K. Żur, J. N. Reddy, Bending, free vibration, and buckling of modified couples stress-based functionally graded porous micro-plates, *Composite Structures,* Vol. 209, pp. 879–888, 2019.

[14] F. Fan, Y. Xu, S. Sahmani, B. Safaei, Modified couple stress-based geometrically nonlinear oscillations of porous functionally graded microplates using NURBS-based isogeometric approach, *Computer Methods in Applied Mechanics and Engineering,* Vol. 372, pp. 113400, 2020.

[15] C. L. Thanh, L. V. Tran, T. Q. Bui, H. X. Nguyen, M. Abdel-Wahab, Isogeometric analysis for size-dependent nonlinear thermal stability of porous FG microplates, *Composite Structures,* Vol. 221, pp. 110838, 2019.

[16] Q. H. Pham, P. C. Nguyen, Dynamic stability analysis of porous functionally graded microplates using a refined isogeometric approach, *Composite Structures,* Vol. 284, pp. 115086, 2022.

[17] N. V. Nguyen, K. Q. Tran, P. Phung-Van, J. Lee, H. Nguyen-Xuan, An isogeometric analysis of functionally graded triply periodic minimal surface microplates, *Aerospace Science and Technology,* Vol. 137, pp. 108270, 2023.

[18] P. Phung-Van, P. T. Hung, H. Nguyen-Xuan, C. H. Thai, Small scale analysis of porosity-dependent functionally graded triply periodic minimal surface nanoplates using nonlocal strain gradient theory, *Applied Mathematical Modelling,* Vol. 127, pp. 439–453, 2024.

[19] P. T. Hung, M. Abdel-Wahab, P. Phung-Van, C. H. Thai, A refined size-dependent modified strain gradient analysis of graphene platelet-reinforced functionally graded triply periodic minimal surface microplates using isogeometric analysis, *Engineering Analysis with Boundary Elements,* Vol. 180, pp. 106442, 2025.

[20] M. E. Gurtin, A. I. Murdoch, A continuum theory of elastic material surfaces, *Archive for Rational Mechanics and Analysis,* Vol. 57, No. 4, pp. 291–323, 1975.

[21] L. Lu, X. Guo, J. Zhao, On the mechanics of Kirchhoff and Mindlin plates incorporating surface energy, *International Journal of Engineering Science,* Vol. 124, pp. 24–40, 2018.

[22] P. Malekzadeh, M. Shojaee, A two-variable first-order shear deformation theory coupled with surface and nonlocal effects for free vibration of nanoplates, *Journal of Vibration and Control,* Vol. 21, No. 14, pp. 2755–2772, 2013.

[23] J. Zhou, P. Lu, Y. Xue, C. Lu, A third-order plate model with surface effect based on the Gurtin–Murdoch surface elasticity, *Thin-Walled Structures,* Vol. 185, pp. 110606, 2023.

[24] L. H. Tong, F. Lin, Y. Xiang, H. S. Shen, C. W. Lim, Buckling analysis of nanoplates based on a generic third-order plate theory with shear-dependent non-isotropic surface stresses, *Composite Structures,* Vol. 265, pp. 113708, 2021.

[25] Y. Gholami, R. Ansari, R. Gholami, H. Rouhi, Analyzing primary resonant dynamics of functionally graded nanoplates based on a surface third-order shear deformation model, *Thin-Walled Structures,* Vol. 131, pp. 487–499, 2018.

[26] M. Shaat, F. F. Mahmoud, X. L. Gao, A. F. Faheem, Size-dependent bending analysis of Kirchhoff nano-plates based on a modified couple-stress theory including surface effects, *International Journal of Mechanical Sciences,* Vol. 79, pp. 31–37, 2014.

[27] B. Zhang, H. Li, J. Liu, H. Shen, X. Zhang, Surface energy-enriched gradient elastic Kirchhoff plate model and a novel weak-form solution scheme, *European Journal of Mechanics - A/Solids,* Vol. 85, pp. 104118, 2021.

[28] S. Liu, T. Yu, L. V. Lich, S. Yin, T. Q. Bui, Size and surface effects on mechanical behavior of thin nanoplates incorporating microstructures using isogeometric analysis, *Computers & Structures,* Vol. 212, pp. 173–187, 2019.

[29] L. Lu, X. Guo, J. Zhao, A unified size-dependent plate model based on nonlocal strain gradient theory including surface effects, *Applied Mathematical Modelling,* Vol. 68, pp. 583–602, 2019.

[30] A. Assadi, H. Najaf, M. Nazemizadeh, Size-dependent vibration of single-crystalline rectangular nanoplates with cubic anisotropy considering surface stress and nonlocal elasticity effects, *Thin-Walled Structures,* Vol. 170, pp. 108518, 2022.

[31] P. Shi, C. Dong, H. Shou, B. Li, Bending, vibration and buckling isogeometric analysis of functionally graded porous microplates based on the TSDT incorporating size and surface effects, *Thin-Walled Structures,* Vol. 191, pp. 111027, 2023.

[32] N. V. Nguyen, D. H. Phan, Assessment of dynamic instability of thin nanoplates considering size and surface energy effects, *Engineering Analysis with Boundary Elements,* Vol. 155, pp. 861–872, 2023.

[33] K. Khorshidi, B. Soltannia, M. Karimi, M. Zakaryaei, Natural frequencies of submerged microplate structures, coupled to stationary fluid, using modified strain gradient theory, *Composite Structures,* Vol. 326, pp. 117583, 2023.

[34] K. Khorshidi, M. Karimi, Analytical modeling for vibrating piezoelectric nanoplates in interaction with inviscid fluid using various modified plate theories, *Ocean Engineering,* Vol. 181, pp. 267–280, 2019.

[35] J. N. Reddy, Analysis of functionally graded plates, *International Journal for Numerical Methods in Engineering,* Vol. 47, No. 1-3, pp. 663–684, 2000.

[36] T. J. R. Hughes, J. A. Cottrell, Y. Bazilevs, Isogeometric analysis: CAD, finite elements, NURBS, exact geometry and mesh refinement, *Computer Methods in Applied Mechanics and Engineering,* Vol. 194, No. 39-41, pp. 4135–4195, 2005.

[37] R. Ansari, V. Mohammadi, M. Faghih Shojaei, R. Gholami, H. Rouhi, Nonlinear vibration analysis of Timoshenko nanobeams based on surface stress elasticity theory, *European Journal of Mechanics - A/Solids,* Vol. 45, pp. 143–152, 2014.

[38] A. Chakrabarti, A. H. Sheikh, Dynamic instability of imperfect laminated sandwich plates with in-plane partial edge load, *Latin American Journal of Solids and Structures,* Vol. 7, No. 4, pp. 457–474, 2010.